

An enhanced slope in the transmission spectrum of the hot Jupiter WASP-104b

G. Chen^{1*}, E. Pallé^{2,3}, H. Parviainen^{2,3}, H. Wang⁴, R. van Boekel⁵,
F. Murgas^{2,3}, F. Yan⁶, V. J. S. Béjar^{2,3}, N. Casasayas-Barris^{2,3}, N. Crouzet⁷,
E. Esparza-Borges³, A. Fukui^{8,2}, Z. Garai^{9,10,11}, K. Kawauchi⁸, S. Kurita⁸,
N. Kusakabe^{13,14}, J. P. de Leon¹⁵, J. Livingston¹⁵, R. Luque^{2,3},
A. Madrigal-Aguado^{2,3}, M. Mori¹⁵, N. Narita^{16,17,13,2}, T. Nishiumi^{18,13},
M. Oshagh^{2,3}, M. Sánchez-Benavente^{2,3}, M. Tamura^{15,13,14}, Y. Terada^{19,20},
N. Watanabe^{18,13}

Affiliations are listed at the end of the paper.

Accepted 2020 November 11. Received 2020 October 31; in original form 2020 August 20

ABSTRACT

We present the optical transmission spectrum of the hot Jupiter WASP-104b based on one transit observed by the blue and red channels of the DBSP spectrograph at the Palomar 200-inch telescope and 14 transits observed by the MuSCAT2 four-channel imager at the 1.52 m Telescopio Carlos Sánchez. We also analyse 45 additional *K2* transits, after correcting for the flux contamination from a companion star. Together with the transit light curves acquired by DBSP and MuSCAT2, we are able to revise the system parameters and orbital ephemeris, confirming that no transit timing variations exist. Our DBSP and MuSCAT2 combined transmission spectrum reveals an enhanced slope at wavelengths shorter than 630 nm and suggests the presence of a cloud deck at longer wavelengths. While the Bayesian spectral retrieval analyses favour a hazy atmosphere, stellar spot contamination cannot be completely ruled out. Further evidence, from transmission spectroscopy and detailed characterisation of the host star’s activity, is required to distinguish the physical origin of the enhanced slope.

Key words: Planetary systems – Planets and satellites: individual: WASP-104b – Planets and satellites: atmospheres – Techniques: spectroscopic – Techniques: photometric

1 INTRODUCTION

Transmission spectroscopy (Seager & Sasselov 2000) has been working exceptionally well in characterising exoplanet atmospheres since the first atmospheric detection (Charbonneau et al. 2002). Due to the slant viewing geometry, it is a very sensitive technique to detect the opacity sources in the limb of an atmosphere (Fortney 2005), resulting in a variety of atomic, ionic, and molecular detections in exoplanet atmospheres (see the review of Madhusudhan 2019, and references therein).

Recent high-precision observations conducted in both space (e.g., Sing et al. 2016; Tsiaras et al. 2018) and ground (e.g., Sedaghati et al. 2017; Nikolov et al. 2018; Chen et al.

2018; Pearson et al. 2019) start to resolve spectral absorption profiles, enabling us to retrieve chemical abundances and atmospheric metallicity. Empirical population studies are also emerging to disentangle the atmospheric metallicity and elemental ratios imprinted by planet formation histories (e.g., Kreidberg et al. 2014; Wakeford et al. 2017a; Pinhas et al. 2019; Welbanks et al. 2019).

To this end, it becomes necessary to understand the role of clouds/hazes in shaping the spectral signatures of transmission spectrum (e.g., Stevenson 2016; Iyer et al. 2016; Heng 2016; Crossfield & Kreidberg 2017; Fu et al. 2017; Gao et al. 2020). Several hot Jupiters have been observed to exhibit transmission spectra dominated by a slope in the optical wavelengths, for example, HAT-P-12b (Alexoudi et al. 2018; Wong et al. 2020), HAT-P-18b (Kirk et al. 2017), HAT-P-32b (Mallonn & Strassmeier 2016; Alam et al. 2020),

* E-mail: guochen@pmo.ac.cn (GC)

HATS-8b (May et al. 2020), HD 189733b (Sing et al. 2011; Pont et al. 2013), TrES-3b (Parviainen et al. 2016), WASP-6b (Jordán et al. 2013; Nikolov et al. 2015; Carter et al. 2020), WASP-12b (Sing et al. 2013), WASP-19b (Sedaghati et al. 2017), WASP-43b (Weaver et al. 2020), WASP-69b (Murgas et al. 2020). Such a slope could be a potential sign of scattering processes in the planetary atmosphere, which could stem from the H_2 molecules, condensates, or photochemical hazes (e.g., Lecavelier Des Etangs et al. 2008; Wakeford & Sing 2015; Wakeford et al. 2017b; Kitzmann & Heng 2018; Pinhas & Madhusudhan 2017; Ohno & Kawashima 2020). However, the absorption of metal lines (Lothringer et al. 2020) and sulfur compounds (Zahnle et al. 2009; Evans et al. 2018), or the contribution of stellar heterogeneity (McCullough et al. 2014; Oshagh et al. 2014; Rackham et al. 2018, 2019) could also induce spectral signatures mimicking a slope at low spectral resolutions.

Transmission spectroscopy has been conducted mostly in planets of relatively low gravity ($\lesssim 15 \text{ ms}^{-2}$), because their atmospheres potentially have larger scale heights to produce more signals. Extending to the regime of intermediate gravity (roughly $20\text{--}50 \text{ ms}^{-2}$) can help understand how gravity influences vertical mixing rates, atmospheric composition, and clouds/hazes (e.g., Komacek et al. 2019; Zhang 2020). Here we report the transmission spectrum for the hot Jupiter WASP-104b ($T_{\text{eq}} \sim 1500 \text{ K}$), which orbits a G8 star every 1.75 days (Smith et al. 2014). With a mass of $\sim 1.3 M_{\text{Jup}}$ and radius of $\sim 1.1 R_{\text{Jup}}$, it has a gravity higher than 20 ms^{-2} . Based on *K2* observations, Močnik et al. (2018) revised the system parameters and found neither signs of transit timing variations (TTVs) nor transit duration variations (TDVs). The *K2* phase curve further revealed that WASP-104b is very dark, with a geometric albedo lower than 0.03 at 95% confidence (Močnik et al. 2018). Garhart et al. (2020) presented secondary eclipse observations of WASP-104b by *Spitzer*, and reported a dayside brightness temperature of $1716 \pm 197 \text{ K}$ in the $3.6 \mu\text{m}$ band and $1783 \pm 205 \text{ K}$ in the $4.5 \mu\text{m}$ band, respectively.

This paper is organised as follows. In Section 2, we present the summary of spectroscopic and photometric observations, and the corresponding data reduction steps. In Section 3, we describe the dilution correction for the flux contamination by a companion star and light-curve modelling processes. In Section 4, we present the revised system parameters and transmission spectrum, and discuss the observed spectral signatures. Finally, we give our conclusions in Section 5.

2 OBSERVATIONS AND DATA REDUCTION

2.1 P200/DBSP spectroscopy

We observed one transit of WASP-104b on the night of 2015 February 13, using the Double Spectrograph (DBSP; Oke & Gunn 1982) installed at the Palomar 200-inch (P200) Hale telescope in California, USA (Program TAP2012B04, PI: G. Chen). A reference star, 2MASS J10422442+0726349, which was ~ 29 arcsec away, was simultaneously observed with the target star WASP-104. They were placed on a slit of length 128 arcsec and width 10 arcsec. The dichroic D48 was used to split light into the blue and red channels at the wavelength

$\sim 4800 \text{ \AA}$. The blue channel employed the $300 \text{ lines mm}^{-1}$ grating, covering a wavelength range of $3250\text{--}4770 \text{ \AA}$ with a dispersion of $2.1 \text{ \AA per pixel}$. The red channel employed the $158 \text{ lines mm}^{-1}$ grating, covering a wavelength range of $4600\text{--}9850 \text{ \AA}$ with a dispersion of $3.0 \text{ \AA per pixel}$. The CCDs for both channels have a format of 4096×2048 unbinned pixels, with a pixel scale of $0.389 \text{ arcsec pix}^{-1}$ for blue and $0.293 \text{ arcsec pix}^{-1}$ for red. The night was clear, with a median seeing of 2.1 arcsec , varying between 1.5 and 2.7 arcsec . The observation started ~ 70 min before the transit ingress and ended ~ 80 min after the transit egress. The exposure times for the blue and red cameras were 60 sec and 150 sec, respectively. The HeNeAr and FeAr arc lamps were observed for the DBSP blue and red channels, respectively, through a 0.5 arcsec narrow slit before and after the science observation, which will be used in the subsequent wavelength calibrations.

We adapted our GTC data reduction procedures to reduce the acquired P200/DBSP data (e.g., Chen et al. 2017a,b, 2018, 2020), which can be generalised to all long-slit data sets. The spectral images were calibrated for over-scan, bias, flat, sky background, and cosmic ray hits. One-dimensional spectra were extracted using the optimal extraction algorithm (Horne 1986), implemented by the APALL procedure in the IRAF¹ package (Tody 1993). Different apertures were tested to minimise the scatter of the resulting white light curves. The final spectra were extracted using an aperture radius of 20.5 pixels for the blue channel and 14 pixels for the red channel. The time stamp was constructed in Barycentric Julian Dates in Barycentric Dynamical Time (BJD_{TDB}; Eastman et al. 2010). The spectra's spatial and spectral drifts, and the full widths at half maximum (FWHM) of the point spread function (PSF) were recorded for subsequent light-curve analysis. We created the white light curves within the passband of $330\text{--}465 \text{ nm}$ for the blue channel, and within $465\text{--}985 \text{ nm}$ for the red channel. The two channels were further divided into groups of spectroscopic passbands, where it contained four passbands in the blue and 16 in the red, respectively. Most of the spectroscopic passbands have a bin width of 30 nm , except for the passbands on the channel edges. An example of the stellar spectra and spectroscopic passbands are shown in Fig. 1.

2.2 TCS/MuSCAT2 photometry

We observed 14 transits of WASP-104b using the four-channel imager MuSCAT2 (Narita et al. 2019) installed at the 1.52 m Telescopio Carlos Sánchez (TCS) in Tenerife, Spain. MuSCAT2 uses three dichroics to split light into four channels, enabling the capability of simultaneous observations in the g , r , i , and z_s bands. It is equipped with four 1024×1024 CCDs to record the images, with a pixel scale of $0.44 \text{ arcsec pix}^{-1}$, resulting in a field of view of $7.4 \times 7.4 \text{ arcmin}^2$. Of the 14 transits, eight were observed in four bands, five were observed in the r , i , and z_s bands, while one was observed in the g and i bands. This results in a total of 49 light curves. The missing channel in some of the transit observations was due to the replacement of a broken CCD. The r band acquired on the night of 2018 April 10

¹ <https://www.iraf.net/>

Table 1. Observation summary.

#	Tele.	Instru.	Start night	Start UT	End UT	Filter	t_{exp} [sec]	Airmass ^a	Aperture [pix]	Weather ^b
1	P200	DBSP	2015-02-13	07:24	11:39	blue, red	60, 150	1.20-1.11-1.44	20.5, 14	A
2	TCS	MuSCAT2	2018-01-12	02:24	06:38	g, r, i, z_s	3, 2, 3, 4	1.21-1.07-1.29	11, 12, 10, 9	A
3	TCS	MuSCAT2	2018-01-26	02:46	06:53	g, r, i, z_s	15, 15, 15, 15	1.09-1.07-1.68	13, 13, 13, 13	C
4	TCS	MuSCAT2	2018-04-10	21:36	01:38	g, r, i, z_s	5, 12, 12, 12	1.10-1.07-1.51	13, 12, 12, 11	A
5	TCS	MuSCAT2	2018-04-17	21:33	01:18	g, r, i, z_s	15, 15, 15, 15	1.08-1.07-1.55	13, 13, 12, 13	A
6	TCS	MuSCAT2	2018-12-01	03:14	06:01	g, i	10, 10	1.90-1.11-1.11	9, 9	A
7	TCS	MuSCAT2	2018-12-08	02:49	06:20	r, i, z_s	10, 15, 15	1.87-1.07-1.07	12, 11, 9	B
8	TCS	MuSCAT2	2018-12-15	03:25	06:47	r, i, z_s	3, 6, 10	1.40-1.07-1.08	9, 11, 8	A
9	TCS	MuSCAT2	2018-12-22	03:34	06:46	r, i, z_s	15, 30, 40	1.25-1.07-1.11	13, 13, 13	B
10	TCS	MuSCAT2	2019-01-28	00:19	04:30	r, i, z_s	4, 7, 14	1.46-1.07-1.12	12, 12, 11	B
11	TCS	MuSCAT2	2019-05-17	20:44	23:43	r, i, z_s	12, 25, 25	1.08-1.08-1.73	9, 9, 9	B
12	TCS	MuSCAT2	2020-02-13	22:46	01:46	g, r, i, z_s	35, 35, 35, 35	1.55-1.09-1.09	10, 13, 13, 13	C
13	TCS	MuSCAT2	2020-03-05	23:42	03:43	g, r, i, z_s	15, 15, 20, 20	1.12-1.07-1.43	12, 8, 12, 13	A
14	TCS	MuSCAT2	2020-03-12	00:52	03:51	g, r, i, z_s	12, 8, 15, 15	1.08-1.08-1.66	10, 11, 9, 9	B
15	TCS	MuSCAT2	2020-03-21	20:10	23:32	g, r, i, z_s	12, 8, 15, 15	1.78-1.07-1.07	12, 12, 11, 10	A

Notes. ^aThe first and third values refer to the airmass at the beginning and at the end of the observation. The second value gives the minimum airmass. ^bWeather conditions: A – Clear; B – Thin cirrus; C – Thick cirrus.

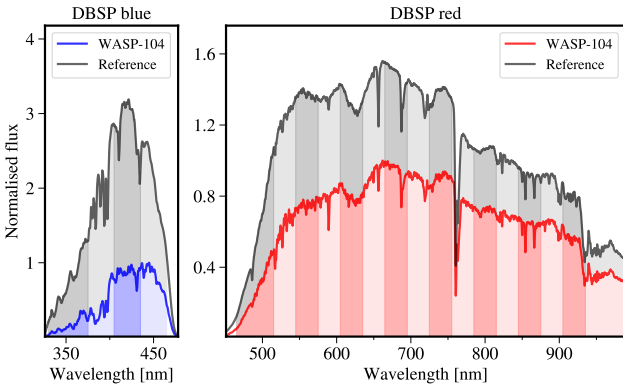


Figure 1. Example stellar spectra observed by P200/DBSP. The left and right panels present the DBSP blue and red spectra, respectively. The spectra are normalised to the maximum of WASP-104’s spectra. Shaded areas show the spectroscopic passbands.

suffered from saturation issues, and related exposures were discarded. Telluric variations can be well corrected by the reference stars in most nights, except for the night of 2020 February 13, where some of the exposures acquired in the cloud-crossing events had to be discarded. A summary of the MuSCAT2 transit observations is given in Table 1.

We adapted the customized routines outlined in Chen et al. (2014) to reduce the MuSCAT2 data, which was originally designed to reduce the data acquired by another multi-colour imaging instrument GROND (Greiner et al. 2008) that can simultaneously conduct observations in the g, r, i, z, J, H, K bands. The raw images were calibrated for bias and flat. Aperture photometry was performed using the APER routine in the IDL DAOPHOT² package. The centroid was determined by first creating a threshold mask on the stars

and then averaging the marginal x, y distributions with flux as weights, respectively. Apertures with a grid of increasing radii were tested to minimize the light-curve scatter, with ten different sky annulus sizes being tested for each radius. Meanwhile, different combinations of reference stars were also tested to search for the optimal reference that can minimize the light-curve scatter. The maximum allowed aperture radius was 13 pixels (i.e., 5.72 arcsec), since there is a companion star in the south at a separation of 6.84 arcsec (see Fig. 2). The chosen aperture radii for the final photometry are given in Table 1. The time stamps for the MuSCAT2 observations were also converted to BJD_{TDB}, referring to the mid-point of exposures.

2.3 K2 photometry

WASP-104 was one of the Campaign 14 targets observed by the K2 mission (Howell et al. 2014). The K2 observations spanned 80 days from 2017 May 31 to August 19, covering 45 transits. They have been analysed and published by Močnik et al. (2018), however, it is unknown whether the flux contamination by the companion star was corrected or not (see Sect. 3.1), and no individual mid-transit times were reported. We therefore downloaded the short cadence target pixel file from Mikulski Archive for Space Telescopes (MAST) using the PYTHON package **lightkurve**³ (Lightkurve Collaboration et al. 2018). A custom aperture mask (see Fig. 2) was created to calculate the Simple Aperture Photometry (SAP) light curve. The systematics were removed using the Pixel Level Decorrelation (PLD; e.g., Deming et al. 2015; Luger et al. 2016, 2018) algorithm implemented by **lightkurve**. Outliers were removed if they were deviating more than 4σ from the 100-point Gaussian-convolved light curve. In the end, 115261 data points remained. Since we were only interested in the transit events,

² <https://idlastro.gsfc.nasa.gov/ftp/pro/idlphot/>

³ <https://github.com/KeplerGO/lightkurve>

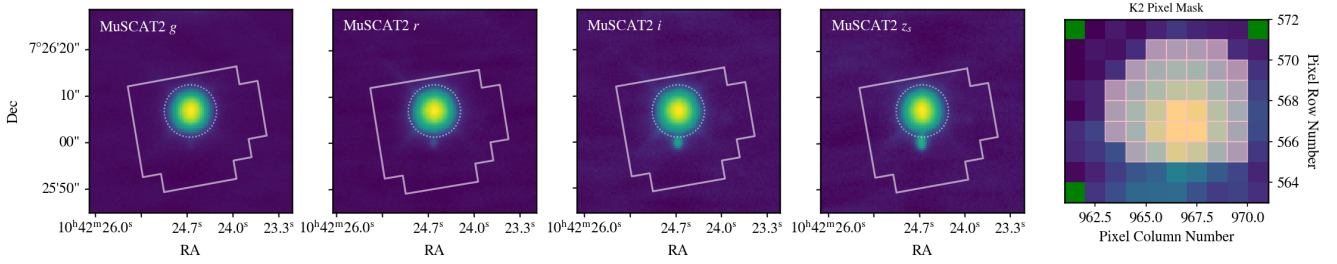


Figure 2. *K2* custom aperture mask on the four MuSCAT2 bands (left four panels) and on the *K2* target pixel file (right panel). The dotted circle refers to a radius of 13 MuSCAT2 pixels. The companion star at a separation of 6.84 arcsec can be clearly seen in the *r*, *i*, *z_s* bands, which is included in the customized *K2* aperture mask. We note that the MuSCAT2 and *K2* images have different orientations.

we splitted the corrected light curve into 0.15 d pieces centered at the mid-transit time of each individual transit event, which contained a total of 9801 data points.

3 ANALYSIS

3.1 Flux contamination from a companion star

As shown in Fig. 2, a faint companion star can be noticed toward the south of WASP-104 in the MuSCAT2 images at a distance of 6.84 arcsec, which is 6.65 mag fainter in the *Gaia* *G* band (Gaia Collaboration et al. 2018). The companion star is more prominent in the *z_s* band, while it is basically invisible in the *g* band, indicating that it is a late type star. It can be spatially resolved in the ground-based observations, thus its contamination could be eliminated for both DBSP and MuSCAT2 observations. However, it is not possible to separate the companion in the aperture mask of the *K2* target pixel file.

We attempted to derive the companion-to-target flux ratio ($F_{\text{comp}}/F_{\star}$) using the out-of-transit spectra obtained with the DBSP red channel. We used the combination of a Moffat function (Moffat 1969) and a Lorentz function to fit for the spatial profile. A single peak is described as follows:

$$F = w \times \text{Moffat} + (1 - w) \times \text{Lorentz}, \quad (1)$$

where F is the flux count and w is the weight. The Moffat and Lorentz components share the same centroid and width. A linear trend was fitted together with the target and companion peaks, to correct for the slope introduced by the PSF wing of the reference star 2MASS J10422442+0726349. The fitting was implemented by the IDL package `mpfit`⁴. An example of the peak fitting is presented in the top panel of Fig. 3. The derived flux-ratio spectrum is shown in the bottom panel of Fig. 3. The uncertainties represent the standard deviation of individually measured flux-ratio spectra. We note that the fitting failed at some wavelengths shorter than 6300 Å, where zero uncertainties were assigned.

We first performed a simple template matching using the empirical library of stellar spectra from the Sloan Digital Sky Survey’s Baryon Oscillation Spectroscopic Survey (Kesseli et al. 2017). An M7V template with a metallicity of

+0.5 for the companion and a G8V template with a metallicity of +0.5 for WASP-104 can best match the measured DBSP flux-ratio spectrum (see the blue line in the bottom panel of Fig. 3). After integrating in the *K2* band using the *Kepler* instrument response function⁵, we derived a flux ratio of 0.1737 per cent.

We then searched for the theoretical spectral templates that can best match the measured flux-ratio spectrum. With certain stellar parameters, e.g., effective temperature T_{eff} , metallicity [Fe/H], and surface gravity $\log g$, we interpolated for WASP-104 and the companion star in the grid of spectral templates obtained from the PHOENIX library⁶ stellar atmospheres (Husser et al. 2013), and convolved the spectra to seeing-limited spectral resolution. The synthetic flux-ratio spectrum was multiplied by a scale factor before it was compared to the data. To fully explore the parameter space, the PYTHON package `emcee`⁷ (Foreman-Mackey et al. 2013) was used to implement the affine-invariant ensemble sampler for Markov chain Monte Carlo (MCMC). During the fitting process, the stellar parameters of WASP-104 were fixed to $T_{\text{eff}} = 5416$ K, [Fe/H] = 0.40, and $\log g = 4.36$ (Sousa et al. 2018), and only the data between 5200 and 9100 Å that have successful flux-ratio measurements were used. As a result, we obtained $T_{\text{eff}} = 2827 \pm 6$ K, [Fe/H] = 0.18 ± 0.03 , and $\log g = 4.46 \pm 0.07$ for the companion star, and the scale factor is $f = 0.128 \pm 0.002$.

Finally, based on the best-fitting synthetic flux-ratio spectrum (see Fig. 3), we calculated a flux ratio of 0.1794 ± 0.0075 per cent for the *K2* band, which is adopted for the dilution correction in the subsequent analysis. The dilution induced by this flux ratio is very small, i.e., $\Delta R_p/R_{\star} = 0.000091$ according to our modelling of 45 *K2* light curves with or without dilution correction. For completeness, we still corrected it in the light-curve modelling. The DBSP and MuSCAT2 light curves were assumed to be free of flux contamination given the carefully limited aperture radius adopted in photometry.

⁵ https://keplergo.arc.nasa.gov/kepler_response_hires1.txt

⁶ <http://phoenix.astro.physik.uni-goettingen.de>

⁷ <https://github.com/dfm/emcee>

⁴ <https://pages.physics.wisc.edu/~craigm/idl/idl.html>

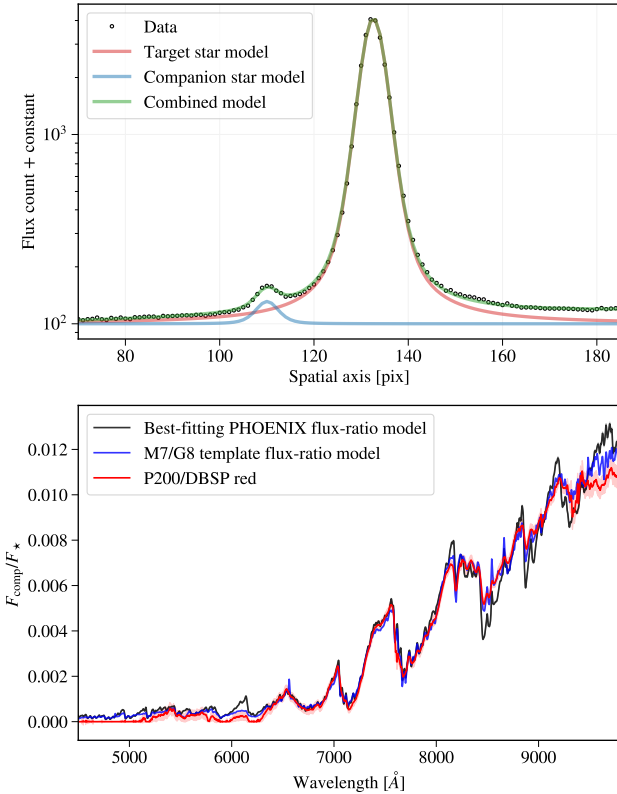


Figure 3. *Top panel:* an illustration of multi-peak fitting to measure the companion-to-target flux ratio. *Bottom panel:* Flux-ratio spectrum between the companion star and WASP-104. Red line and shaded area show the measured flux ratios derived from P200/DBSP’s out-of-transit data. The black line is the best-fitting PHOENIX flux-ratio model. The blue line is the flux-ratio model created from the empirical M7 and G8 spectral templates.

3.2 Light-curve modelling

We have created two broadband light curves from one DBSP transit, 49 broadband light curves from 14 MuSCAT2 transits, and 45 broadband light curves from 45 *K2* transits. These amount to a total of 96 broadband light curves. We have also created one set of spectroscopic light curves from the DBSP observation. The broadband light curves will be used to derive common transit parameters such as inclination, semi-major axis, and mid-transit time, while the spectroscopic light curves will be used to derive the transmission spectrum.

In general, the transit model is constructed by the Mandel & Agol (2002) analytic model, implemented by the PYTHON package `batman`⁸ (Kreidberg 2015). The transit model is diluted by a flux ratio of F_{comp}/F_* if the flux contamination exists. The systematics are accounted by Gaussian processes (GP; Rasmussen & Williams 2006; Gibson et al. 2012), implemented by the PYTHON packages `george`⁹ (Ambikasaran et al. 2015). The covariance between the vari-

ables x_α is given by the Matérn $\nu = 3/2$ kernel¹⁰

$$k_{ij} = A^2 \left(1 + \sqrt{3 D_{ij}^2} \right) \exp \left(-\sqrt{3 D_{ij}^2} \right), \quad (2)$$

where $D_{ij}^2 = \sum_{\alpha=1}^N (\hat{x}_{\alpha,i} - \hat{x}_{\alpha,j})^2 / L_\alpha^2$, and A and L_α are the characteristic correlation amplitude and length scale. The adopted GP input x_α will be described in the subsections. The transit model is adopted as the GP mean function. A white-noise jitter is added to the photon-noise dominated spectro-/photometric uncertainties in quadrature to account for potential uncertainty underestimation.

The transit model was parameterised by orbital period P , orbital inclination i , scaled semi-major axis a/R_* , radius ratio R_p/R_* , mid-transit time T_C , limb-darkening coefficients u_i , orbital eccentricity e , and argument of periastron ω . The orbital period was fixed to a value of 1.75540636 d from Močnik et al. (2018), while the eccentricity was fixed to zero (Smith et al. 2014). The quadratic limb-darkening law was adopted, and the coefficients were fitted with Gaussian priors $\mathcal{N}(u_i, \sigma^2)$, except for $K2$, in which they are freely fitted. The prior mean values u_i were calculated from the ATLAS9 stellar atmosphere models¹¹ using a public PYTHON package¹² (Espinoza & Jordán 2015), with the stellar parameters of $T_{\text{eff}} = 5500$ K, $\log g = 4.5$, and $[\text{Fe}/\text{H}] = 0.3$. The prior standard deviations σ were assumed as the average gap between the $T_{\text{eff}} = 5500$ K, $T_{\text{eff}} = 5250$ K, and $T_{\text{eff}} = 5750$ K grids. The other transit parameters always had uniform priors, while the GP hyperparameters had log uniform priors.

The posterior distributions are explored using MCMC implemented by `emcee` (Foreman-Mackey et al. 2013). Each fitting process always consists of two runs of short chains for the “burn-in” phase before a long chain is started. The number of walkers and length of chains depend on how many (hyper-)parameters are fitted and whether or not a convergence can be achieved.

3.2.1 Fitting of broadband light curves

For some nights in which short exposures (e.g., ~ 3 sec) were employed, the number of data points in one light curve could be as large as 2300. Given the large number of light curves and data points and different sources of systematics, a global fitting of all the 96 broadband light curves using GP would be computationally expensive. Instead, we adopted the following way to fit for the broadband light curves.

- **K2.** The 45 *K2* transit light curves were fitted individually. Time sequence was used as the only input in the GP kernel. Consequently, the free parameters were orbital inclination i , scaled semi-major axis a/R_* , radius ratio R_p/R_* , mid-transit time T_C , limb-darkening coefficients (u_1 , u_2), white noise jitter, and GP hyperparameters ($\ln A$, $\ln L_t$).

¹⁰ The Matérn $\nu = 3/2$ kernel is a “rougher” generalisation of the squared exponential kernel, which results in smoother functions of the inputs than the latter (Gibson et al. 2012). We tested both kernels and obtained consistent results, confirming that the kernel choice is not critical for our data sets. Following Gibson et al. (2013)’s tests, we adopted the Matérn $\nu = 3/2$ kernel.

¹¹ <http://kurucz.harvard.edu/grids.html>

¹² <https://github.com/nespinoza/limb-darkening>

⁸ <https://github.com/lkreidberg/batman>

⁹ <https://github.com/dfm/george>

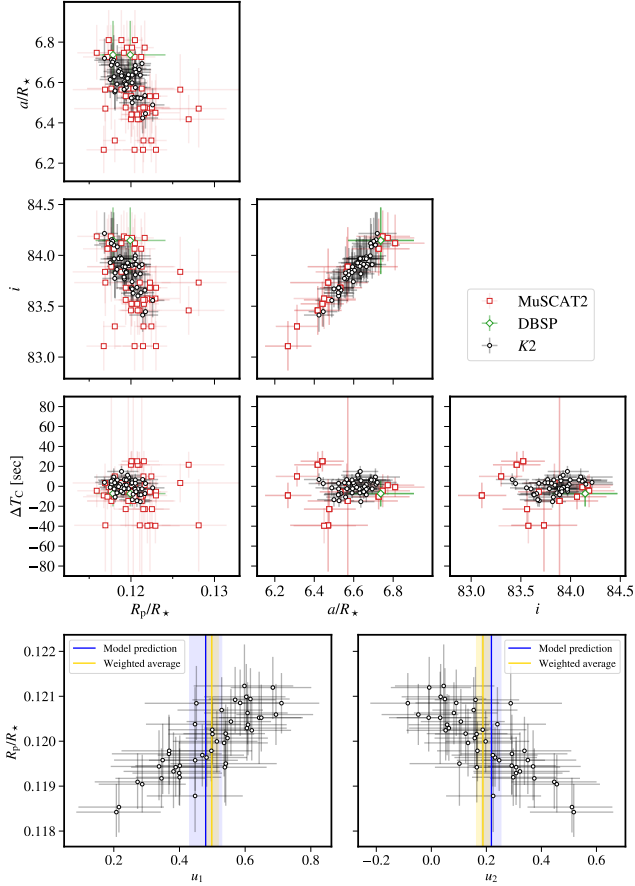


Figure 4. Correlation between pairs of transit parameters measured in individual light curves. Red squares, green diamond, and black circles refer to the measurements from MuSCAT2, DBSP, and K2, respectively.

- **MuSCAT2.** The 49 MuSCAT2 transit light curves were first binned in 2 min intervals individually, and then jointly fitted on a nightly basis. As such, it can reduce the computation cost and take advantage of multi colours to mitigate degeneracy in the parameter space of common transit parameters. Multi-dimensional inputs were used for the GP kernel, including time sequence, target star’s centroid x and y , and PSF’s FWHM s . For each night, the multi-colour light curves were jointly fitted, sharing the same i , a/R_* , and T_C . The other transit parameters (R_p/R_* , u_1 , u_2), white noise jitter, and GP hyperparameters ($\ln A$, $\ln L_t$, $\ln L_x$, $\ln L_y$, $\ln L_s$) were light curve dependent.

- **DBSP.** The two broadband light curves of the DBSP blue and red channels were jointly fitted. The same multi-dimensional GP inputs as those of MuSCAT2 were used. The two light curves shared the same i , a/R_* , and T_C , but different R_p/R_* , limb-darkening coefficients (u_1 , u_2), white noise jitter, and GP hyperparameters ($\ln A$, $\ln L_t$, $\ln L_x$, $\ln L_y$, $\ln L_s$).

From the described analyses, we derived a group of i , a/R_* , R_p/R_* , and ΔT_C , where ΔT_C is the deviation from the linear ephemeris based T_C . Unsurprisingly, as shown in Fig. 4, a clear correlation exists between i and a/R_* . Correlation can also be observed between R_p/R_* and i , or between

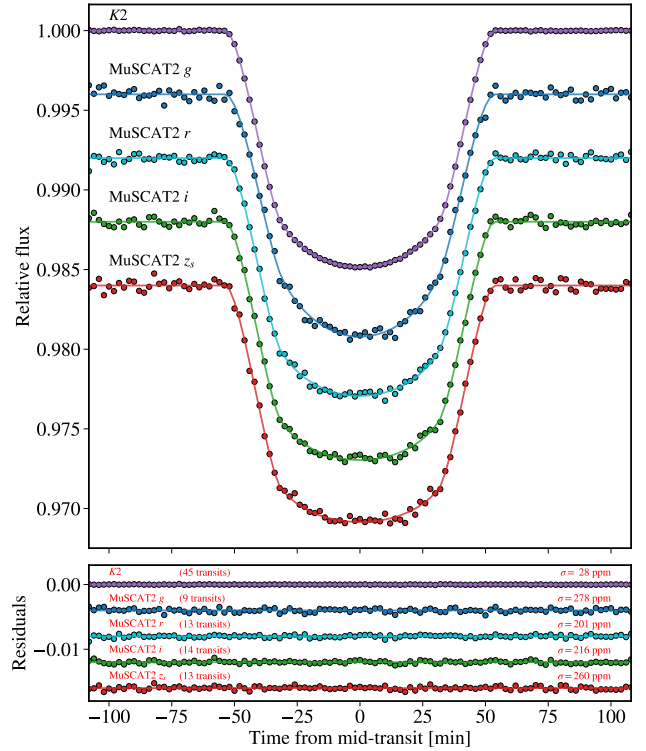


Figure 5. Phase-folded K2 and MuSCAT2 light curves, where systematics have been corrected. The light curves have been added constant offsets and binned in 2 min intervals for display clarify.

R_p/R_* and a/R_* , while they are not evident between ΔT_C and other transit parameters. The correlations are more evident for the K2 measurements due to higher photometric precision. The K2 limb-darkening coefficients cannot be constrained in a single transit and exhibit clear correlation with R_p/R_* . However, the weighted average values of all 45 transits are consistent with the predictions based on stellar atmosphere models. This indicates that the Gaussian priors imposed on the MuSCAT2 and DBSP data are reasonable. We calculated the weighted average values for i and a/R_* , and list them in Table 2. The MuSCAT2 and DBSP weighted average values agree with those of K2 within 2σ .

To eliminate the correlation’s impact on the derived wavelength dependent radius ratios, we performed the light-curve modelling again for the K2, MuSCAT2, and DBSP light curves. For this time, the values of i and a/R_* were fixed to those weighted average values listed in Table 2, and T_C was fixed to those determined in the previous step (see Table A1). Since i and a/R_* were fixed to the same values, the light curves were fitted individually for either K2, or MuSCAT2, or DBSP blue and red. We note that the original unbinned MuSCAT2 light curves were used for this particular analysis. Finally, for each band, the radius ratio values were weighted averaged, and given in Table 3.

The phase-folded K2 and MuSCAT2 light curves are shown in Fig. 5. The 49 unbinned MuSCAT2 light curves are presented in Fig. 6. The two DBSP broadband light curves are presented in Fig. 7. From the modelling of the broadband light curves, the standard deviation of unbinned light-curve residuals is $1.00\text{--}2.43\times$ photon noise for MuSCAT2, $2.12\times$

Table 2. Common transit parameters derived from this work.

Case	i [deg]	a/R_*
$K2$ +MuSCAT2+DBSP (adopted)	83.811 ± 0.025	6.591 ± 0.012
$K2$	83.827 ± 0.027	6.599 ± 0.012
MuSCAT2+DBSP	83.713 ± 0.068	6.527 ± 0.035

Table 3. Derived transit parameters for the WASP-104 system.

Parameter	Value
Radius ratio, R_p/R_* ^a	
$K2$	0.11992 ± 0.00011
MuSCAT2 g	0.12098 ± 0.00046
MuSCAT2 r	0.12002 ± 0.00030
MuSCAT2 i	0.12031 ± 0.00026
MuSCAT2 z_s	0.11998 ± 0.00033
DBSP blue	$0.1222^{+0.0035}_{-0.0034}$
DBSP red	$0.11896^{+0.00073}_{-0.00084}$
Orbital inclination, i [deg]	83.811 ± 0.025
Scaled semi-major axis, a/R_*	6.591 ± 0.012
Transit duration, T_{14} [d]	0.074109 ± 0.000063
Ingress(egress) duration, T_{12} [d]	0.014907 ± 0.000071
Impact parameter, b	0.7147 ± 0.0014
Transit epoch, T_0 [MJD] ^b	7935.070228 ± 0.000011
Orbital period, P [d]	$1.75540563 \pm 0.00000011$

Notes. ^aThe presented values of R_p/R_* are weighted average of each band, derived from the analyses where i , a/R_* , and T_C were fixed. ^bMJD = BJD_{TDB} - 2450000.

photon noise for DBSP blue, $5.81 \times$ photon noise for DBSP red, and 0.85 – $1.01 \times$ photon noise for $K2$, respectively. When phase-folded into 2 min intervals, the light-curve residuals show an RMS of 28 ppm for $K2$ (45 transits), 278 ppm for MuSCAT2 g (9 transits), 201 ppm for MuSCAT2 r (13 transits), 216 ppm for MuSCAT2 i (14 transits), and 260 ppm for MuSCAT2 z_s (13 transits).

3.2.2 Fitting of spectroscopic light curves

To derive the DBSP transmission spectrum for WASP-104b, we performed light-curve modelling on the DBSP spectroscopic light curves. The transit parameters i and a/R_* were fixed to the weighted average values listed in Table 2. The mid-transit time was fixed to the one derived from the DBSP joint fitting as described in Sect. 3.2.1 (see Table A1).

We tested various state vectors as the GP inputs, individually or in combination, such as time sequence t , spectra's drift in the spectral and spatial directions (x, y) , and PSF's FWHM s , and calculated corresponding Bayesian information criterion (BIC; Schwarz 1978) and Akaike information criterion (AIC; Akaike 1974). The combination (t, x, y, s) resulted in the lowest AIC value, while (t, y, s) resulted in the lowest BIC value. The transmission spectra derived from

Table 4. Transmission spectrum measured by P200/DBSP.

#	Wavelength (nm)	R_p/R_*
1	330 – 375	$0.12198^{+0.00192}_{-0.00213}$
2	375 – 405	$0.12199^{+0.00134}_{-0.00111}$
3	405 – 435	$0.12023^{+0.00096}_{-0.00090}$
4	435 – 465	$0.12133^{+0.00124}_{-0.00191}$
5	465 – 515	$0.11731^{+0.00182}_{-0.00182}$
6	515 – 545	$0.11841^{+0.00105}_{-0.00105}$
7	545 – 575	$0.11900^{+0.00090}_{-0.00097}$
8	575 – 605	$0.11906^{+0.00094}_{-0.00100}$
9	605 – 635	$0.11842^{+0.00050}_{-0.00052}$
10	635 – 665	$0.11718^{+0.00028}_{-0.00029}$
11	665 – 695	$0.11733^{+0.00045}_{-0.00047}$
12	695 – 725	$0.11824^{+0.00037}_{-0.00039}$
13	725 – 755	$0.11765^{+0.00053}_{-0.00053}$
14	755 – 785	$0.11838^{+0.00069}_{-0.00072}$
15	785 – 815	$0.11736^{+0.00097}_{-0.00085}$
16	815 – 845	$0.11750^{+0.00072}_{-0.00067}$
17	845 – 875	$0.11652^{+0.00089}_{-0.00087}$
18	875 – 905	$0.11622^{+0.00108}_{-0.00146}$
19	905 – 935	$0.11849^{+0.00084}_{-0.00093}$
20	935 – 985	$0.11850^{+0.00096}_{-0.00130}$

these two GP input combinations exhibit almost no difference ($\chi^2 = 0.05$ for 20 degrees of freedom, hereafter dof). We also tested using only the transit model as the GP mean function, as well as multiplying the transit model by a baseline trend. The results were consistent, but the latter exhibited higher AIC and BIC values. For our final choice, we adopted the transit model as the GP mean function, and (t, y, s) as the GP inputs. The free parameters were radius ratio R_p/R_* , limb-darkening coefficients (u_1, u_2), white noise jitter, and GP hyperparameters ($\ln A$, $\ln L_t$, $\ln L_y$, $\ln L_s$).

We first performed the light-curve modelling directly on the original DBSP spectroscopic light curves. We then derived the common-mode noise in a way slightly different from previous studies (e.g., Chen et al. 2018, 2020; Murgas et al. 2019, 2020), due to strong flux variation across wavelengths. The spectroscopic light curves were divided by their best-fitting transit model individually. The resulting light-curve systematics residuals were averaged for the DBSP blue and red channels, respectively. The average common-mode systematics empirical model was then corrected in the original spectroscopic light curves. The common-mode corrected spectroscopic light curves were fitted to derive the final transmission spectrum. The transmission spectrum derived from the common-mode corrected data set is consistent with the one derived from the original data set ($\chi^2 = 8.0$ for 20 dof), but with smaller error bars because the achromatic common-mode systematics trend has been removed.

The DBSP spectroscopic light curves are presented in Fig. 8. The derived DBSP transmission spectrum is given in Table 4. For the DBSP spectroscopic light curves, the standard deviation of light-curve residuals is 1.2 – $2.2 \times$ pho-

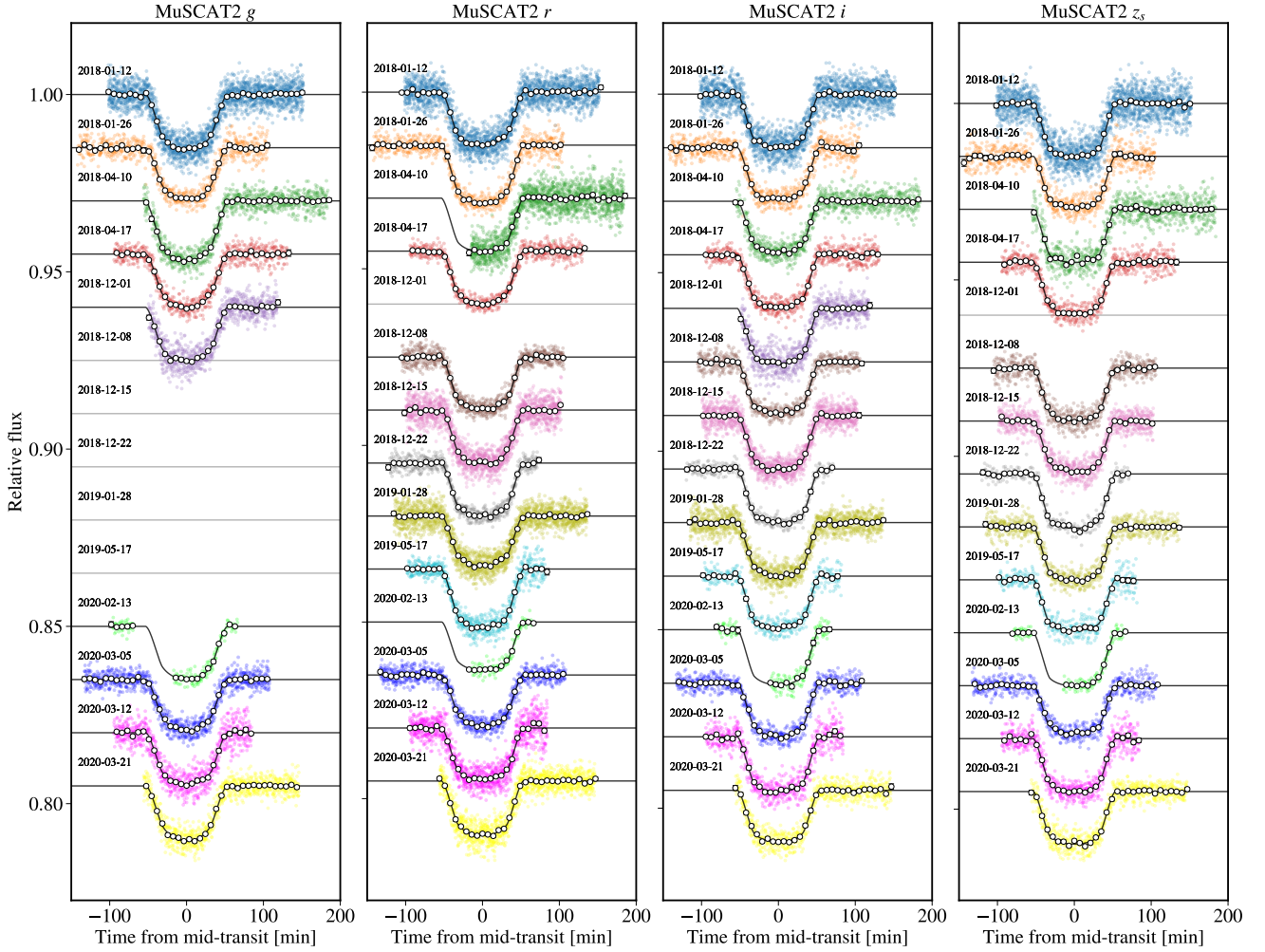


Figure 6. Multi-colour light curves obtained with TCS/MuSCAT2 on 14 nights. From *left to right* shows the systematics corrected light curves in the *g*, *r*, *i*, *z_s* bands, respectively. The colour dots refer to the original unbinned exposures, while the black circles refer to light curves binned in 7 min intervals for display purpose.

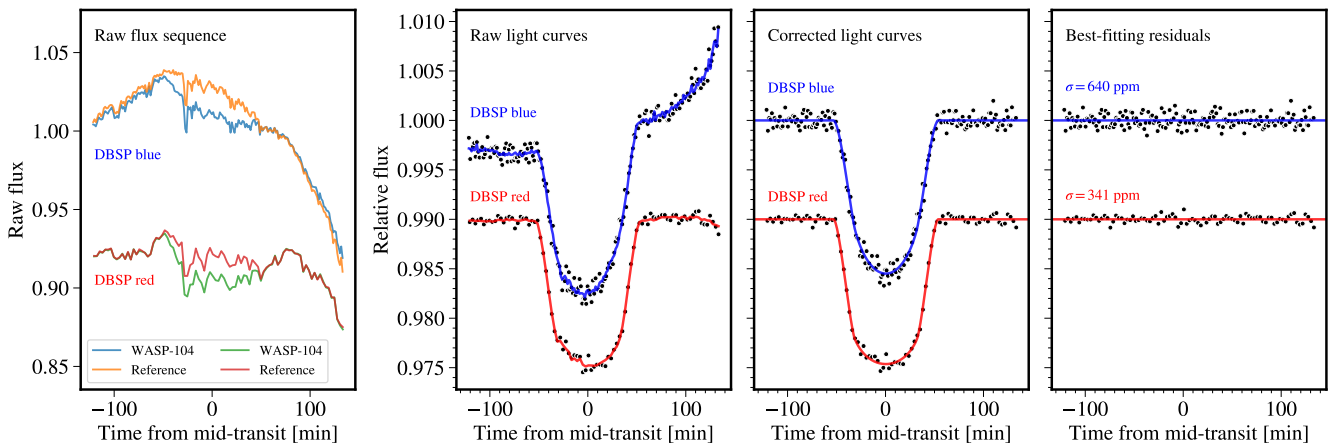


Figure 7. Broadband light curves obtained with the P200/DBSP blue and red channels on the night of 2015 February 13. The *left panel* presents the raw flux sequences of the target and reference stars. The three *right panels* present the reference-calibrated light curves: before systematics correction, after systematics correction, and best-fitting residuals.

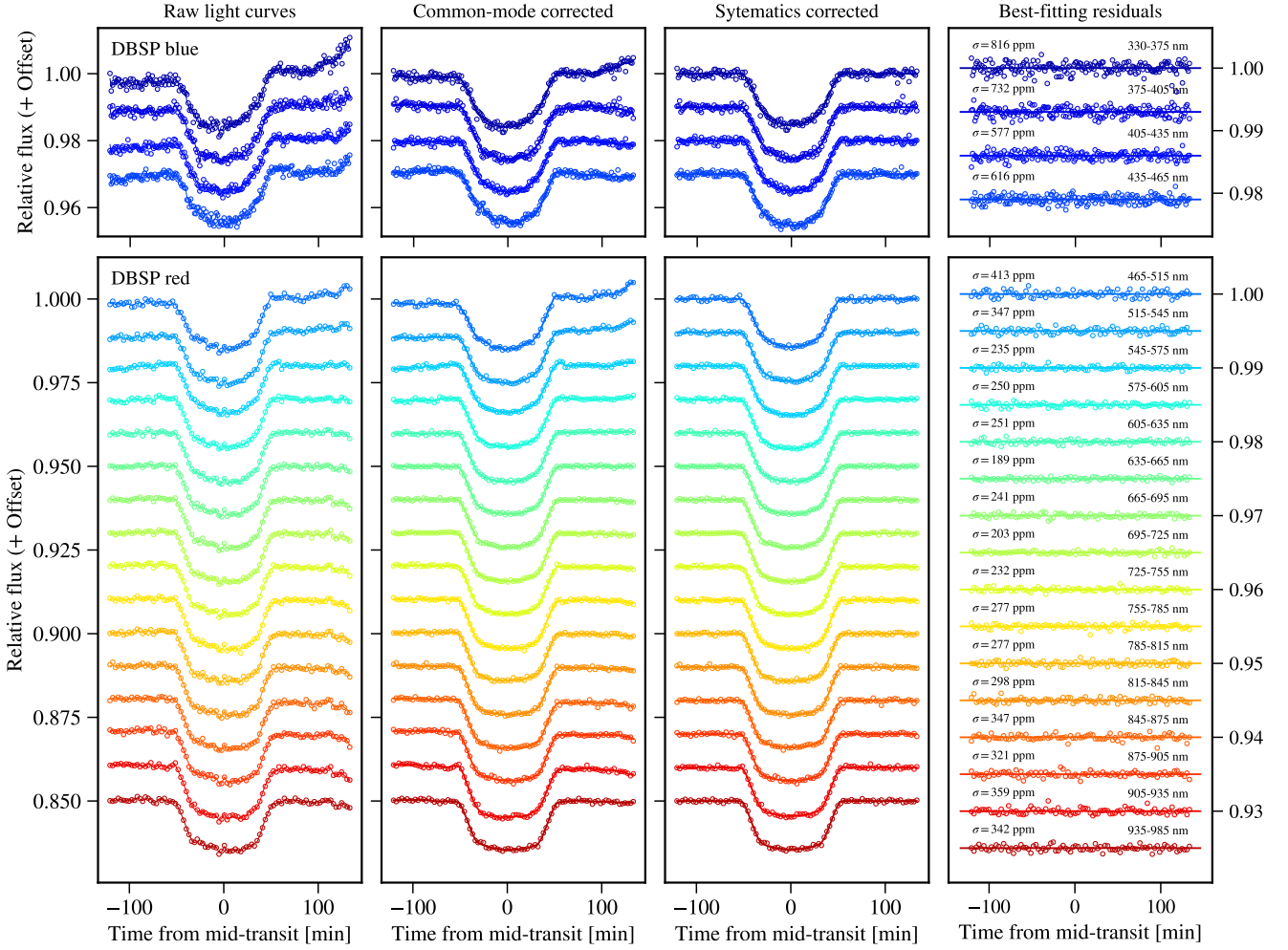


Figure 8. Spectroscopic light curves obtained with P200/DBSP on the night of 2015 February 13. The two rows show the light curves from the DBSP blue and red channels, respectively. From *left to right* presents the reference-calibrated raw light curves, common-mode noise corrected light curves, systematics corrected light curves, and best-fitting residuals, respectively.

ton noise, and it decreases to $0.9\text{--}1.4\times$ photon noise after removing the common-mode noise.

In addition to DBSP, we have derived a broadband transmission spectrum from the MuSCAT2 multi-colour light curves in the second step described in Sect. 3.2.1. As can be seen in Fig. 9, the spectral shape of the MuSCAT2 broadband transmission spectrum agrees well with DBSP when the latter is binned into the same bandpasses. However, there is a constant offset of $\Delta R_p/R_\star = 0.00234 \pm 0.00022$ between these two transmission spectra.

4 RESULTS AND DISCUSSION

4.1 Revised system parameters

4.1.1 Transit parameters and TTVs

Based on the newly collected MuSCAT2 and DBSP light curves and the re-analysed *K2* light curves, we are able to revise the transit parameters for the WASP-104 planetary system, which are presented in Table 3.

As shown in Table 2, we have obtained consistent values for i and a/R_\star between *K2* and MuSCAT2+DBSP. However, our inclination $i = 83.811^\circ \pm 0.025^\circ$ and impact parameter $b = 0.7147 \pm 0.0014$ are deviating more than 5σ from those ($83.612^\circ \pm 0.026^\circ$, 0.7278 ± 0.0016) of Močnik et al. (2018). Therefore, we also recalculated the transit duration $T_{14} = 0.074109 \pm 0.000063$ d and the ingress (or egress) duration $T_{12} = 0.014907 \pm 0.000071$ d using the equations (2) and (3) from Seager & Mallén-Ornelas (2003). Again, the differences are significant ($\Delta T_{14} = 1.85 \pm 0.11$ min and $\Delta T_{12} = -0.66 \pm 0.15$ min) from those of Močnik et al. (2018). Given that we have more light curves observed in different colours, we report our newly revised parameters.

To revise the transit ephemeris, we re-measured the mid-transit times for four TRAPPIST and two Euler transit light curves from Smith et al. (2014). The light curves were fitted individually, and the GP was implemented by *george* with the Matérn $\nu = 3/2$ kernel, where only the time sequence was adopted as the GP input. Consequently, there are a total of 66 unique mid-transit time measurements, including 45 *K2*, 1 DBSP, 14 MuSCAT2, 4 TRAPPIST, and

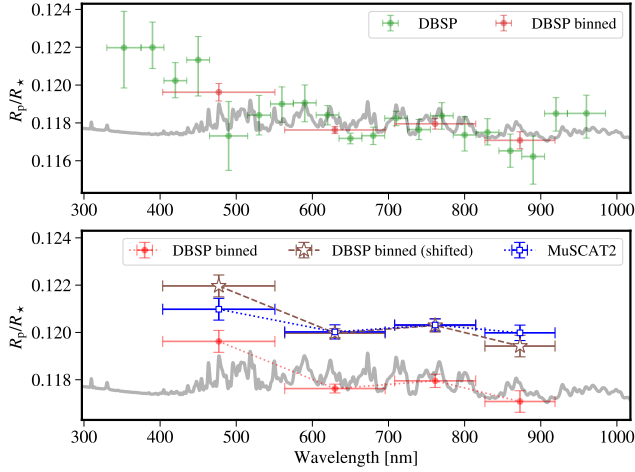


Figure 9. *Top panel:* Original DBSP transmission spectrum (in green) compared to the one binned into the MuSCAT2 bandpasses (in red). A $1\times$ solar cloud-free model is also shown, calculated by PLATON (see Sect. 4.2.2) with WASP-104b’s physical parameters. *Bottom panel:* Comparison between MuSCAT2 and DBSP, where the latter has been shifted upwards by $\Delta R_p/R_* = 0.00234$ (in brown). The MuSCAT2 data are shown in blue.

2 Euler, which are presented in Table A1. We fitted a linear ephemeris to the 66 mid-transit times using *emcee*, where an error multiple was adopted to rescale the error bars of the mid-transit times. This resulted in a reduced chi-square of $\chi^2_\nu = 1.36$ based on the original error bars. The residuals have a standard deviation of 19.5 sec.

Figure 10 presents the mid-transit time residuals assuming the best-fitting linear ephemeris. For comparison, we derived the transit ephemeris based on the *K2* data only or the MuSCAT2 data only, respectively. The two individually derived transit ephemerides are well consistent with each other as can be seen in the zoom-in views of Fig. 10. In particular, the MuSCAT2-based ephemeris is rather precise, thanks to a broader time coverage. Therefore, the current observations do not reveal any significant transit timing variations, confirming the conclusion of Moćnik et al. (2018).

4.1.2 Physical parameters

To revise the physical parameters, we performed a joint analysis of radial velocities (RV), transits, stellar evolution tracks and spectral energy distribution (SED) using the IDL package EXOFASTv2¹³ (Eastman et al. 2013, 2019). We collected 21 RV measurements by the CORALIE and SOPHIE spectrographs presented in the discovery paper (Smith et al. 2014). To reduce the computation cost, we only used the light curves of *K2*, MuSCAT2 *g*, *r*, *i*, *z*, and phase-folded them in 1 min intervals individually, after removing the best-fitting noise models determined in Sect 3.2. We assumed a circular orbit for WASP-104b. We used the MIST stellar evolutionary models (Dotter 2016), and adopted the latest spectroscopic stellar parameters of $T_{\text{eff}} = 5416 \pm 86$ K and $[\text{Fe}/\text{H}] = 0.40 \pm 0.06$ from Sousa et al. (2018) as priors. Other

Table 5. Derived physical parameters for the WASP-104 system from EXOFASTv2.

Symbol	Parameter and unit	Value
Stellar Parameters:		
M_*	Mass [M_\odot]	1.016 ± 0.033
R_*	Radius [R_\odot]	0.935 ± 0.010
L_*	Luminosity [L_\odot]	0.645 ± 0.014
ρ_*	Density [cgs]	1.7515 ± 0.0081
$\log g_*$	Surface gravity [cgs]	4.5032 ± 0.0050
T_{eff}	Effective temperature [K]	5348 ± 32
$[\text{Fe}/\text{H}]$	Metallicity [dex]	0.410 ± 0.057
<i>Age</i>	Age [Gyr]	$2.3^{+2.1}_{-1.5}$
<i>d</i>	Distance [pc]	186.4 ± 1.3
K_*	RV semi-amplitude [m s^{-1}]	201.4 ± 5.8
Planetary Parameters:		
M_p	Mass [M_{Jup}]	1.216 ± 0.045
R_p	Radius [R_{Jup}]	1.093 ± 0.012
ρ_p	Density [cgs]	1.158 ± 0.037
$\log g_p$	Surface gravity [cgs]	3.403 ± 0.013
g_p	Surface gravity [m s^{-2}]	25.26 ± 0.74
T_{eq}	Equilibrium temperature [K]	1474 ± 9
<i>a</i>	Semi-major axis [AU]	0.02864 ± 0.00031
$\langle F \rangle$	Incident Flux [$10^9 \text{ erg s}^{-1} \text{ cm}^{-2}$]	1.070 ± 0.025

priors were the parallax value of 5.34 ± 0.04 mas from *Gaia* DR2 (Gaia Collaboration et al. 2018) and a V-band extinction upper limit of 0.09176 mag from Schlafly & Finkbeiner (2011). For the SED fitting, we used magnitudes measured in *B*, *V*, *g*, *r*, *i* from the URAT1 catalog (Zacharias et al. 2015), *J*, *H*, *K* from the 2MASS catalog (Cutri et al. 2003), and *W1*, *W2*, *W3* from the AllWISE catalog (Cutri & et al. 2014).

Table 5 presents the physical parameters derived from the posterior distributions sampled by EXOFASTv2. In general, these parameters agree well with those reported by Moćnik et al. (2018), except for the planet mass, which is probably a typo (i.e., $1.211 M_{\text{Jup}}$ instead of $1.311 M_{\text{Jup}}$) in Moćnik et al. (2018).

4.2 Transmission spectrum

The DBSP transmission spectrum does not reveal any significant excess absorption at Na, K, or other atoms or molecules that are expected to be common in hot Jupiter atmospheres. When comparing the MuSCAT2 transmission spectrum to that of DBSP, they show the same overall spectral shape, except for a constant offset of $\Delta R_p/R_* = 0.00234 \pm 0.00022$ between them. This offset could be introduced by the rotational modulation of the host star, which requires a flux variability at the ~ 4 per cent level. However, Moćnik et al. (2018) found a rotational modulation with a semi-amplitude of ~ 0.04 percent from the *K2* data. Considering the large time separation, it could also be due to a stellar cycle of 8–10 yr. Another possibility would be due to different sys-

¹³ <https://github.com/jdeast/EXOFASTv2>

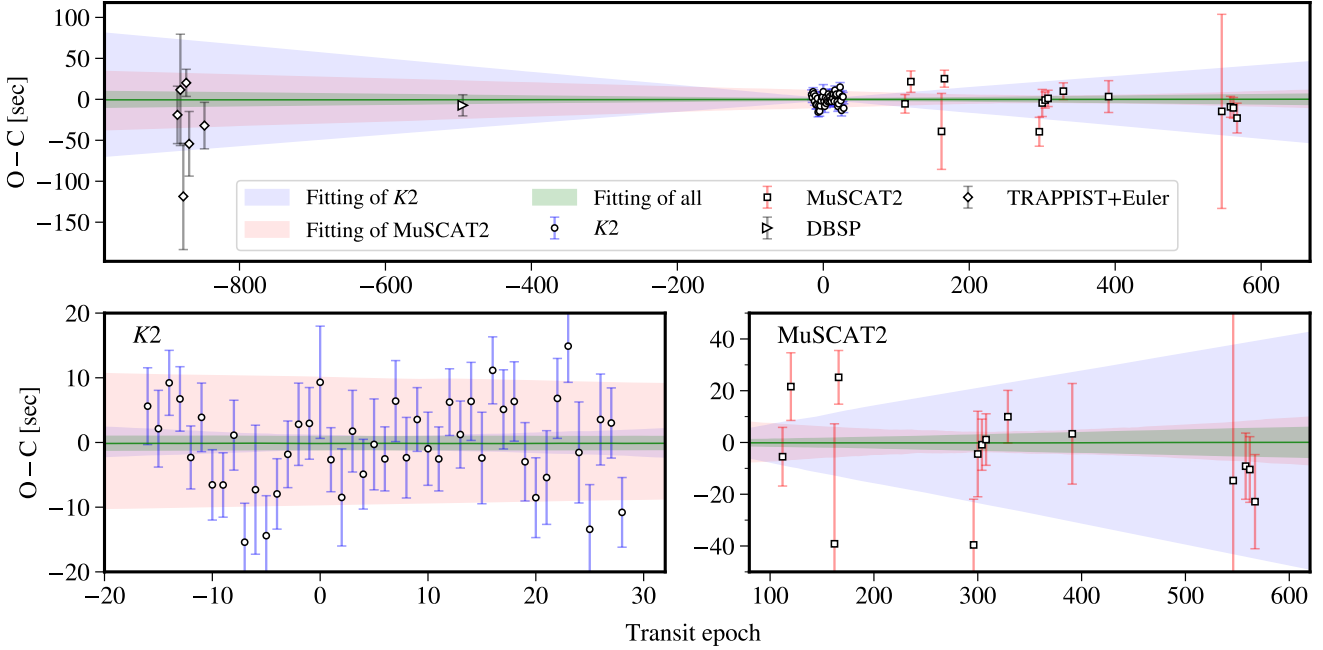


Figure 10. Residuals of the mid-transit times after a linear ephemeris regression. *Top panel* shows all the mid-transit times derived from this work, which include the newly observed DBSP and MuSCAT2 data, and the re-analysed K2, TRAPPIST, and Euler data (Smith et al. 2014; Močnik et al. 2018). *Bottom panel* shows the zoom-in views on the K2 (*bottom left*) and MuSCAT2 (*bottom right*) measurements. The green shaded area present the 1σ confidence region of the fitting on all the available data. In contrast, the blue and red shaded areas present the 1σ confidence regions of the fittings on the K2-only and MuSCAT2-only data, respectively.

tematics, which could potentially bias the measurements. In particular, there is only one DBSP transit observation.

4.2.1 Comparison to simplified model assumptions

Allowing a constant offset correction on the DBSP data, the DBSP and MuSCAT2 combined transmission spectrum of WASP-104b is very similar to that of the puffy hot Jupiter WASP-31b (Gibson et al. 2017). The latter has a low gravity of 4.56 ms^{-1} (Anderson et al. 2011) and exhibits an enhanced slope (Welbanks et al. 2019; Ohno & Kawashima 2020) at wavelengths shorter than $\sim 530 \text{ nm}$ and a cloud deck at longer wavelengths. Following Gibson et al. (2017), we consider the model assumptions: (i) a flat-line model, (ii) a sloped-line model, and (iii) a two-component model (i.e., sloped- and flat-lines for the shorter and longer wavelengths, respectively). In all three cases, the DBSP offset is a free parameter. We performed the model fitting using the PYTHON package `PyMultiNest`¹⁴ (Buchner et al. 2014), which relies on the MultiNest library (Feroz et al. 2009). This package implements the multimodal nested sampling algorithm, and allows us to calculate the model evidence $\ln \mathcal{Z}$. As shown in Table 6, the two-component model is significantly preferred over the flat-line model ($\Delta \ln \mathcal{Z} = 9.7$) and the sloped-line model ($\Delta \ln \mathcal{Z} = 6.4$).

The observed slope of a transmission spectrum can be linked to the index α (also known as the scattering slope in some studies, e.g., Zhang et al. 2019) through $dR_p/d \ln \lambda =$

αH if it is assumed to originate from the power law scattering cross section $\kappa = \kappa_0(\lambda/\lambda_0)^\alpha$ (Lecavelier Des Etangs et al. 2008), where $H = k_B T / (\mu g_p)$ is the scale height. Consequently, the index α can be derived as:

$$\alpha = \frac{\mu g_p R_\star}{k_B T} \frac{dR_p/R_\star}{d \ln \lambda}, \quad (3)$$

where k_B is Boltzmann constant. We adopted $\mu = 2.3 \text{ g mol}^{-1}$ for the mean molecular weight, and obtained the values of g_p , $T (= T_{\text{eq}})$, R_\star from Table 5. As a result, we derived a scattering slope of $\alpha = -7.3 \pm 1.9$ over the whole optical wavelength range based on the sloped-line model, and $\alpha = -17.6^{+3.7}_{-3.9}$ for the wavelengths shorter than $\sim 630 \text{ nm}$ based on the two-component model.

4.2.2 Retrieval assuming planetary atmosphere

In the following subsections, we perform spectral retrieval analyses on the DBSP and MuSCAT2 combined transmission spectrum, to explore the hazy atmosphere scenario and the spot contamination scenario.

We first use the PYTHON package `PLATON`¹⁵ (Zhang et al. 2019, 2020) to perform the spectral retrieval analysis. This package assumes equilibrium chemistry models computed with `GGchem` (Woitke et al. 2018), and allows two free parameters (metallicity Z and C/O ratio) to specify the atmospheric composition. The clouds and hazes are parameterised as a gray absorption at the pressure P_{cloud} and a

¹⁴ <https://johannesbuchner.github.io/PyMultiNest>

¹⁵ <https://github.com/ideasrule/platon>

Table 6. Bayesian model comparison.

Model	$\ln \mathcal{Z}$	$\chi^2_{\text{MAP}}^a$	dof	Description
<i>i</i>	151.161	48.9	22	Flat-line model
<i>ii</i>	154.426	33.9	21	Sloped-line model
<i>iii</i>	160.854	21.4	20	Two-component model
<i>iv</i>	–	–	–	petitRADTRANS , no spot
	165.907	13.2	13	Full model
	165.808	16.3	14	No H ₂ O
	166.807	13.9	14	No TiO
	166.239	13.1	14	No VO
	165.940	14.5	14	No Na
	164.591	17.0	14	No K
<i>v</i>	162.004	19.7	16	PLATON , no spot
<i>vi</i>	160.207	23.0	20	PLATON , pure spot

Notes. ^a χ^2 for the Maximum a Posteriori (MAP) model.

power law cross section (with a scattering slope of α and an enhancement factor A_{scatt} over nominal H₂ Rayleigh scattering), respectively. In addition, DBSP offset ($\Delta D_{\text{DBSP}} = \Delta R_p^2/R_\star^2$), isothermal temperature T and planet radius R_p at 1 bar are free parameters as well.

We also use the PYTHON package **petitRADTRANS**¹⁶ (Mollière et al. 2019) to perform another run of spectral retrieval analysis. This package allows us to specify atmospheric composition in terms of individual atoms and molecules. We use a similar clouds and hazes parameterisation, except that the scattering amplitude is expressed in the form of opacity in units of $\text{cm}^2 \text{g}^{-1}$. The included opacity sources are H₂O, TiO, VO, Na, K, and their mass fractions are free parameters. The remaining free parameters are: isothermal temperature T , reference pressure P_0 (corresponding to white-light radius), and DBSP offset ΔD_{DBSP} .

For both retrieval runs, we employ **PyMultiNest** to perform the fitting processes. The resulting statistics and parameters are listed in Tables 6 and 7. The retrieved models and confidence regions are shown in Fig. 11, and corresponding posterior distributions are given in Fig. A1 and Fig. A2.

The two retrieval runs resulted in consistent results. No atoms or molecules can be detected under current data precision, although the data disfavour TiO but favour K tentatively at $\sim 2\sigma$ level. Similarly, the C/O ratio and metallicity cannot be constrained given the absence of significant spectral features. This indicates that it is very challenging to detect the atmospheres of planets with intermediate surface gravity ($\sim 25 \text{ m s}^{-2}$ in the case of WASP-104b), because their atmospheres are relatively compact and will require much higher data precision to resolve spectral features.

Table 7. Parameters derived from spectral retrieval analyses.

Parameters	petitRADTRANS	PLATON	
		no spot	pure spot
T [K]	1966^{+479}_{-422}	1969^{+604}_{-623}	–
R_p [R_J]	–	$1.078^{+0.006}_{-0.012}$	$1.098^{+0.005}_{-0.005}$
$\log P_0$ [bar]	$-0.06^{+0.95}_{-0.83}$	–	–
$\log P_{\text{cloud}}$ [bar]	$-0.55^{+1.6}_{-1.7}$	$-1.3^{+2.1}_{-1.5}$	–
α	$-16.6^{+3.1}_{-2.3}$	$-17.2^{+3.3}_{-1.9}$	–
$\log A_{\text{scatt}}^a$	$1.63^{+0.83}_{-0.88}$	$-2.0^{+1.5}_{-1.2}$	–
C/O	–	$1.38^{+0.41}_{-0.68}$	–
$\log Z/Z_\odot$	–	$0.27^{+1.14}_{-0.88}$	–
$\log X_{\text{H}_2\text{O}}$	$-4.3^{+2.7}_{-3.6}$	–	–
$\log X_{\text{TiO}}$	$-8.4^{+1.0}_{-1.0}$	–	–
$\log X_{\text{VO}}$	$-8.3^{+1.3}_{-1.1}$	–	–
$\log X_{\text{Na}}$	$-5.7^{+2.7}_{-2.7}$	–	–
$\log X_{\text{K}}$	$-3.1^{+1.5}_{-2.1}$	–	–
T_{spot} [K]	–	–	5163^{+79}_{-191}
f_{spot}	–	–	$0.26^{+0.17}_{-0.11}$
ΔD_{DBSP} [ppm]	-539^{+48}_{-48}	-560^{+48}_{-48}	-586^{+51}_{-52}

Notes. ^aFor **petitRADTRANS**, $f_{\text{scatt}} = \kappa_0$ is a physical quantity. For **PLATON**, f_{scatt} is a dimensionless enhancement factor over the nominal H₂ Rayleigh scattering.

4.2.3 Retrieval assuming stellar heterogeneity

We also perform a third spectral retrieval analysis with **PLATON**, where the planet is assumed to have no atmosphere and the spot contamination is fully responsible for the variation in wavelength dependent transit depths. The adopted free parameters are planet radius R_p , DBSP offset ΔD_{DBSP} , spot temperature T_{spot} , and spot coverage f_{spot} . The spot contamination is implemented by **PLATON** using

$$D_{\lambda,c} = D_\lambda \frac{S(\lambda, T_{\text{phot}})}{f_{\text{spot}} S(\lambda, T_{\text{spot}}) + (1 - f_{\text{spot}}) S(\lambda, T_{\text{phot}})}, \quad (4)$$

where D_λ is the uncontaminated true transit depth at the wavelength λ , $T_{\text{phot}} = 5348 \text{ K}$ is the adopted temperature for unspotted stellar photosphere, and $S(\lambda, T)$ are the interpolated BT-NextGen (AGSS2009) stellar models (Allard et al. 2012).

The retrieved models are shown in the third row of Fig. 11. The retrieved parameters are given in Table 7, and their posterior distributions in Fig. A3. The best retrieved models indicate that the spot temperature is $185^{+79}_{-191} \text{ K}$ lower than the photosphere and that the spot coverage is 26^{+17}_{-11} per cent. The retrieved spot temperature does not follow the trend observed for active giants and dwarfs that hotter photospheres have larger spot-photosphere temperature contrasts (Berdyugina 2005). Should it follow the trend, with a photosphere temperature of 5348 K, the spot temperature would be $\sim 1500 \text{ K}$ lower than the photosphere.

¹⁶ <https://gitlab.com/mauricemolli/petitRADTRANS>

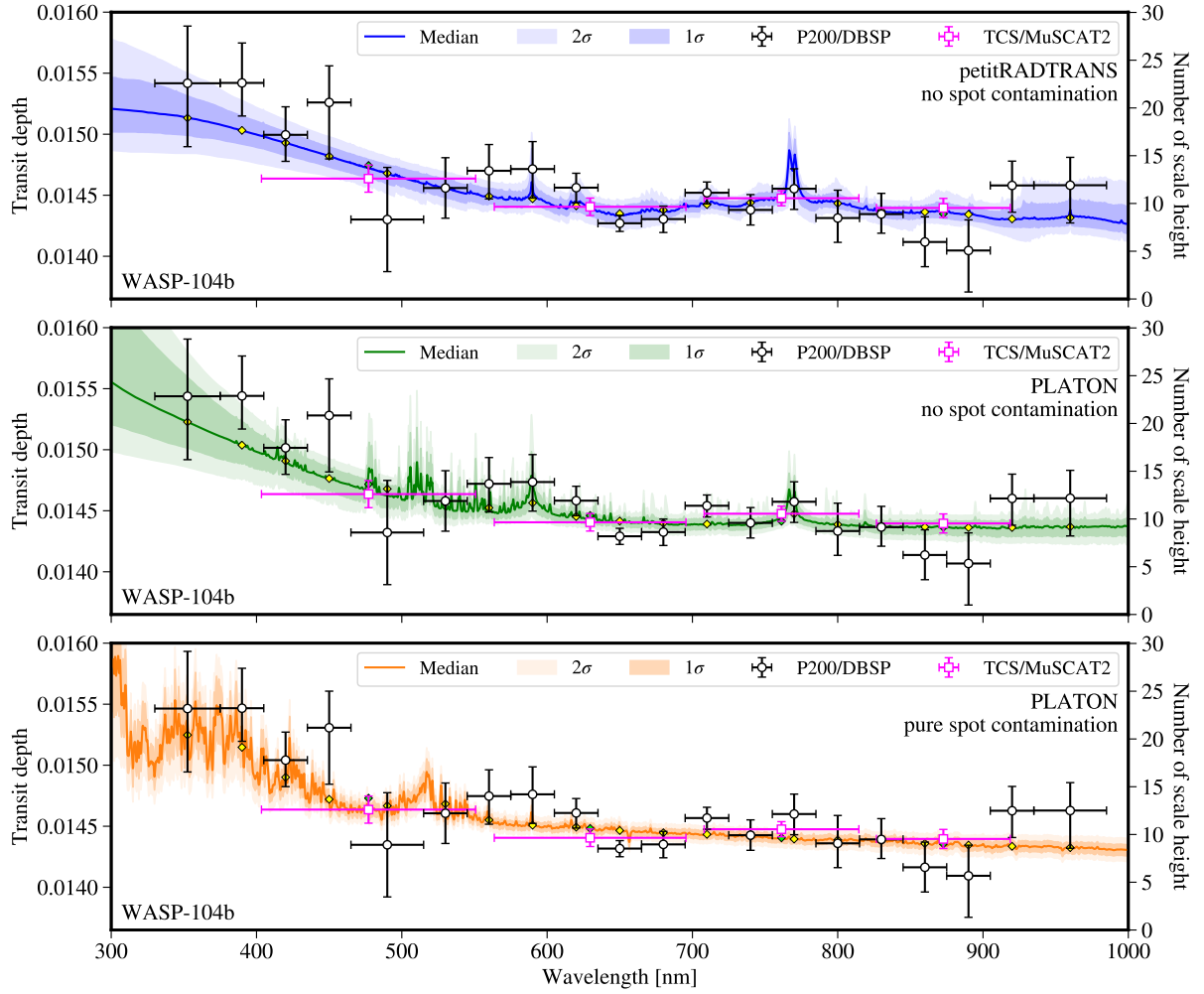


Figure 11. Transmission spectrum of the hot Jupiter WASP-104b. The transit depths measured by P200/DBSP and TCS/MuSCAT2 are shown as black circles and magenta squares, respectively. *Top panel* presents the retrieval analysis performed using the *petitRADTRANS* package (Mollière et al. 2019), where the planetary atmosphere is assumed to induce any spectral features in the measurements. *Middle* and *bottom* panels present the retrieval analyses performed using the *PLATON* package (Zhang et al. 2019, 2020), where the contribution of spot contamination is excluded (*middle panel*) or is the only cause of transit-depth variation (*bottom panel*). For all three panels, the DBSP spectrum has been corrected for the overall offset determined in each retrieval analysis.

4.2.4 Interpretation of the slope

WASP-104b is one of the few transiting planets with intermediate gravity for which a transmission spectrum has been measured. Although the regime of intermediate gravity is barely studied, the current sample tends to show super steep scattering slopes, such as HD 189733b (21.5 ms^{-2} ; Sing et al. 2011; Pont et al. 2013), TrES-3b (27.4 ms^{-2} ; Parviainen et al. 2016), and WASP-43b (47 ms^{-2} ; Weaver et al. 2020). Super steep scattering slopes have also been observed in some hot Jupiters with low gravity. For example, Evans et al. (2018) found that WASP-121b (9.4 ms^{-2}) shows a steep slope at $\lambda \leq 470 \text{ nm}$ and suggested SH as the absorber. May et al. (2020) observed extremely large and variable slopes ($\alpha \sim -100, -40$) in two transits of HATS-8b (4.5 ms^{-2}) which are difficult to explain. For several of the planets with super steep scattering slopes, the debate is open on whether potential spot contamination induced by their active host stars can be underlying responsible physical mechanism, including HD 189733b (McCullough et al.

2014), WASP-43b (Weaver et al. 2020), and WASP-19b (Espinoza et al. 2019).

In our spectral retrieval analyses, both spot contamination and hazy atmosphere models can fit WASP-104b’s transmission spectrum reasonably well, although the Bayesian model comparison (Table 6) favours the hazy atmosphere models. On the other hand, WASP-104 does not show any signs of significant stellar activity (Smith et al. 2014; Močnik et al. 2018), only exhibiting a rotational modulation with a semi-amplitude of $\sim 400 \text{ ppm}$. Should the slope be induced by the spots, with a derived coverage of 26^{+17}_{-11} percent, the spots have to be small and uniformly distributed or contain a large fraction of non-modulating component to avoid inducing large flux variability (Rackham et al. 2018, 2019; Rosich et al. 2020). This is consistent with the fact that none of our observed transit light curves have revealed any significant spot-crossing events, nor have the 45 *K2* transit light curves of higher precision. With a large set of observations dispersed in three years, the MuS-

CAT2 multi-colour transit depths should have averaged out the variation of spot contamination. Since the MuSCAT2 spectral shape is consistent with that of DBSP, spots of similar properties would have to be persistent for at least five years. The large spot coverage would indicate a young age for the host star (e.g., [Morris 2020](#)), which is not favoured by the low lithium abundance ([Smith et al. 2014](#)) and the slow rotation period (~ 23 or ~ 46 days; [Močnik et al. 2018](#)). However, although the full set of evidences point out that the observed slope is not likely caused by spot contamination, we suggest to acquire further evidence, through follow-up transmission spectroscopy and detailed characterisation of the host star's activity, to completely rule out its possibility.

While in theory spot contamination could result in a wide range of slope values, planetary atmospheres can exhibit steep slope values only under certain conditions. [Pinhas & Madhusudhan \(2017\)](#) suggest that a small number of sulphide condensates of modal sizes $\sim 10^{-2} \mu\text{m}$ could introduce very steep slopes. For example, MnS could result in a slope as steep as -13 . But a recent study shows that metal sulphide clouds are strongly inhibited due to nucleation energy barriers ([Gao et al. 2020](#)). On the other hand, photochemical haze can also potentially steepen the scattering slope if eddy diffusion is efficient and the haze mass flux is moderate ([Kawashima & Ikoma 2019](#); [Ohno & Kawashima 2020](#)). Planets with equilibrium temperatures of 1000-1500 K are suggested to be potential targets for super-Rayleigh slopes generated by photochemical haze. With an equilibrium temperature of 1474 ± 9 K, WASP-104b falls into this temperature range, and would be in a location very close to WASP-31b in the figure 5 of [Ohno & Kawashima \(2020\)](#). According to [Ohno & Kawashima \(2020\)](#), the observed slope of WASP-104b could be introduced by tholin at a haze mass flux of $F \sim 10^{-12} \text{ g cm}^2 \text{ s}^{-1}$ and an eddy diffusion of $K_z \sim 10^{-9} \text{ cm}^2 \text{ s}^{-1}$.

5 CONCLUSIONS

We acquired 51 broadband light curves of WASP-104b by observing one transit of WASP-104b with the blue and red channels of the low-resolution spectrograph DBSP at the Palomar 200-inch telescope, and 14 transits with the multi-colour imager MuSCAT2 at the 1.52 m Telescopio Carlos Sánchez. We derived the flux contamination by the companion star close to WASP-104 using the DBSP spectra. We re-analysed the 45 $K2$ transit light curves after considering the dilution correction. Based on the collection of DBSP, MuSCAT2, and $K2$ light curves, we were able to update the transit parameters and physical parameters. We confirm that the planet does not exhibit any transit timing variations.

We further divided the DBSP spectra into chromatic passbands. The resulting DBSP transmission spectrum reveals an enhanced slope at wavelengths shorter than ~ 630 nm and a relatively flat spectrum at longer wavelengths. The broadband transmission spectrum acquired by MuSCAT2 is consistent with that of DBSP in the overall spectral shape except for a constant offset. We performed spectral retrieval analyses on the DBSP and MuSCAT2 combined transmission spectrum using two different publicly available codes, and the results were in a broad agreement. To find the underlying physical cause of the measured slope,

we explored the scenarios where the slope is caused by the planet's atmosphere or by spot contamination. We find that stellar spot contamination is a less likely explanation given the knowledge about the host star's activity and the statistics from the Bayesian spectral retrieval analyses. However, further evidence is required to completely rule out the possibility of spot contamination.

Hot Jupiters with relatively high gravity, like WASP-104b, are rarely studied in transmission spectroscopy. Thus their observational signatures of gravity on clouds/hazes are still not well studied, especially in the upper atmospheres. A combination of better ground-based transit measurements, such as the one performed here, and the extraordinary precision of the *James Webb* space telescope in the coming years, will hopefully allow us to explore and understand this population.

ACKNOWLEDGEMENTS

G. C. acknowledges the support by the B-type Strategic Priority Program of the Chinese Academy of Sciences (Grant No. XDB41000000), the National Natural Science Foundation of China (Grant No. 42075122), the Natural Science Foundation of Jiangsu Province (Grant No. BK20190110), and the Minor Planet Foundation of the Purple Mountain Observatory. This work is partly financed by the Spanish Ministry of Economics and Competitiveness through grants PGC2018-098153-B-C31 and PID2019-109522GB-53. This work is partly supported by JSPS KAKENHI Grant Numbers JP18H01265, JP18H05439, JP17H04574, and JST PRESTO Grant Number JPMJPR1775. M.T. is supported by JSPS KAKENHI Grant Numbers 18H05442, 15H02063, and 22000005. This work is partly supported by Grant-in-Aid for JSPS Fellows, Grant Number JP20J21872. Z.G. was supported by the VEGA grant of the Slovak Academy of Sciences No. 2/0031/18, by the Hungarian NKFI grant No. K-119517 and the GINOP No. 2.3.2-15-2016-00003 of the Hungarian National Research, Development and Innovation Office, and by the City of Szombathely under agreement No. 67.177-21/2016. The authors thank the anonymous referee for constructive comments on the manuscript.

This work uses data obtained through the Telescope Access Program (TAP), which has been funded by the National Astronomical Observatories, Chinese Academy of Sciences, and the Special Fund for Astronomy from the Ministry of Finance. Observations obtained with the Hale Telescope at Palomar Observatory were obtained as part of an agreement between the National Astronomical Observatories, Chinese Academy of Sciences, and the California Institute of Technology. This work is partly based on observations made with the MuSCAT2 instrument, developed by ABC, at Telescopio Carlos Sánchez operated on the island of Tenerife by the IAC in the Spanish Observatorio del Teide. This work includes data collected by the Kepler mission and obtained from the MAST data archive at the Space Telescope Science Institute (STScI). Funding for the Kepler mission is provided by the NASA Science Mission Directorate. STScI is operated by the Association of Universities for Research in Astronomy, Inc., under NASA contract NAS 5-26555. This work has made use of data from the European Space Agency (ESA) mission *Gaia* (<https://www.cosmos.esa.int/gaia>),

processed by the *Gaia* Data Processing and Analysis Consortium (DPAC, <https://www.cosmos.esa.int/web/gaia/dpac/consortium>). Funding for the DPAC has been provided by national institutions, in particular the institutions participating in the *Gaia* Multilateral Agreement. This work has made use of Matplotlib (Hunter 2007), the VizieR catalog access tool, CDS, Strasbourg, France (Ochsenbein et al. 2000), and TEPcat (Southworth 2011).

DATA AVAILABILITY

The data underlying this article will be shared on reasonable request to the corresponding author. The reduced light curves presented in this work will be made available at the CDS (<http://cdsarc.u-strasbg.fr/>).

REFERENCES

- Akaike H., 1974, *IEEE Transactions on Automatic Control*, **19**, 716
- Alam M. K., et al., 2020, *AJ*, **160**, 51
- Alexoudi X., et al., 2018, *A&A*, **620**, A142
- Allard F., Homeier D., Freytag B., 2012, *Philosophical Transactions of the Royal Society of London Series A*, **370**, 2765
- Ambikasaran S., Foreman-Mackey D., Greengard L., Hogg D. W., O’Neil M., 2015, *IEEE Transactions on Pattern Analysis and Machine Intelligence*, **38**, 252
- Anderson D. R., et al., 2011, *A&A*, **531**, A60
- Berdyugina S. V., 2005, *Living Reviews in Solar Physics*, **2**, 8
- Buchner J., et al., 2014, *A&A*, **564**, A125
- Carter A. L., et al., 2020, *MNRAS*, **494**, 5449
- Charbonneau D., Brown T. M., Noyes R. W., Gilliland R. L., 2002, *ApJ*, **568**, 377
- Chen G., et al., 2014, *A&A*, **563**, A40
- Chen G., Pallé E., Nortmann L., Murgas F., Parviainen H., Nowak G., 2017a, *A&A*, **600**, L11
- Chen G., Guenther E. W., Pallé E., Nortmann L., Nowak G., Kunz S., Parviainen H., Murgas F., 2017b, *A&A*, **600**, A138
- Chen G., et al., 2018, *A&A*, **616**, A145
- Chen G., Casasayas-Barris N., Pallé E., Welbanks L., Madhusudhan N., Luque R., Murgas F., 2020, *A&A*, **642**, A54
- Crossfield I. J. M., Kreidberg L., 2017, *AJ*, **154**, 261
- Cutri R. M., et al. 2014, VizieR Online Data Catalog, [p. II/328](#)
- Cutri R. M., et al., 2003, VizieR Online Data Catalog, [p. II/246](#)
- Deming D., et al., 2015, *ApJ*, **805**, 132
- Dotter A., 2016, *ApJS*, **222**, 8
- Eastman J., Siverd R., Gaudi B. S., 2010, *PASP*, **122**, 935
- Eastman J., Gaudi B. S., Agol E., 2013, *PASP*, **125**, 83
- Eastman J. D., et al., 2019, arXiv e-prints, [p. arXiv:1907.09480](#)
- Espinoza N., Jordán A., 2015, *MNRAS*, **450**, 1879
- Espinoza N., et al., 2019, *MNRAS*, **482**, 2065
- Evans T. M., et al., 2018, *AJ*, **156**, 283
- Feroz F., Hobson M. P., Bridges M., 2009, *MNRAS*, **398**, 1601
- Foreman-Mackey D., Hogg D. W., Lang D., Goodman J., 2013, *PASP*, **125**, 306
- Fortney J. J., 2005, *MNRAS*, **364**, 649
- Fu G., Deming D., Knutson H., Madhusudhan N., Mandell A., Fraine J., 2017, *ApJ*, **847**, L22
- Gaia Collaboration et al., 2018, *A&A*, **616**, A1
- Gao P., et al., 2020, *Nature Astronomy*, **4**, 137
- Garhart E., et al., 2020, *AJ*, **159**, 137
- Gibson N. P., Aigrain S., Roberts S., Evans T. M., Osborne M., Pont F., 2012, *MNRAS*, **419**, 2683
- Gibson N. P., Aigrain S., Barstow J. K., Evans T. M., Fletcher L. N., Irwin P. G. J., 2013, *MNRAS*, **428**, 3680
- Gibson N. P., Nikolov N., Sing D. K., Barstow J. K., Evans T. M., Kataria T., Wilson P. A., 2017, *MNRAS*, **467**, 4591
- Greiner J., et al., 2008, *PASP*, **120**, 405
- Heng K., 2016, *ApJ*, **826**, L16
- Horne K., 1986, *PASP*, **98**, 609
- Howell S. B., et al., 2014, *PASP*, **126**, 398
- Hunter J. D., 2007, *Computing in Science and Engineering*, **9**, 90
- Husser T. O., Wende-von Berg S., Dreizler S., Homeier D., Reiners A., Barman T., Hauschildt P. H., 2013, *A&A*, **553**, A6
- Iyer A. R., Swain M. R., Zellem R. T., Line M. R., Roudier G., Rocha G., Livingston J. H., 2016, *ApJ*, **823**, 109
- Jordán A., et al., 2013, *ApJ*, **778**, 184
- Kawashima Y., Ikoma M., 2019, *ApJ*, **877**, 109
- Kesseli A. Y., West A. A., Veyette M., Harrison B., Feldman D., Bochanski J. J., 2017, *ApJS*, **230**, 16
- Kirk J., Wheatley P. J., Louden T., Doyle A. P., Skillen I., McCormac J., Irwin P. G. J., Karjalainen R., 2017, *MNRAS*, **468**, 3907
- Kitzmann D., Heng K., 2018, *MNRAS*, **475**, 94
- Komacek T. D., Showman A. P., Parmentier V., 2019, *ApJ*, **881**, 152
- Kreidberg L., 2015, *PASP*, **127**, 1161
- Kreidberg L., et al., 2014, *ApJ*, **793**, L27
- Lecavelier Des Etangs A., Pont F., Vidal-Madjar A., Sing D., 2008, *A&A*, **481**, L83
- Lightcurve Collaboration et al., 2018, Lightkurve: Kepler and TESS time series analysis in Python (ascl:1812.013)
- Lothringer J. D., Fu G., Sing D. K., Barman T. S., 2020, *ApJ*, **898**, L14
- Luger R., Agol E., Kruse E., Barnes R., Becker A., Foreman-Mackey D., Deming D., 2016, *AJ*, **152**, 100
- Luger R., Kruse E., Foreman-Mackey D., Agol E., Saunders N., 2018, *AJ*, **156**, 99
- Madhusudhan N., 2019, *ARA&A*, **57**, 617
- Mallon M., Strassmeier K. G., 2016, *A&A*, **590**, A100
- Mandel K., Agol E., 2002, *ApJ*, **580**, L171
- May E. M., Gardner T., Rauscher E., Monnier J. D., 2020, *AJ*, **159**, 7
- McCullough P. R., Crouzet N., Deming D., Madhusudhan N., 2014, *ApJ*, **791**, 55
- Moffat A. F. J., 1969, *A&A*, **3**, 455
- Mollière P., Wardenier J. P., van Boekel R., Henning T., Molaverdikhani K., Snellen I. A. G., 2019, *A&A*, **627**, A67
- Morris B. M., 2020, *ApJ*, **893**, 67
- Močnik T., Hellier C., Southworth J., 2018, *AJ*, **156**, 44
- Murgas F., Chen G., Pallé E., Nortmann L., Nowak G., 2019, *A&A*, **622**, A172
- Murgas F., Chen G., Nortmann L., Pallé E., Nowak G., 2020, *A&A*, **641**, A158
- Narita N., et al., 2019, *Journal of Astronomical Telescopes, Instruments, and Systems*, **5**, 015001
- Nikolov N., et al., 2015, *MNRAS*, **447**, 463
- Nikolov N., et al., 2018, *Nature*, **557**, 526
- Ochsenbein F., Bauer P., Marcot J., 2000, *A&AS*, **143**, 23
- Ohno K., Kawashima Y., 2020, *ApJ*, **895**, L47
- Oke J. B., Gunn J. E., 1982, *PASP*, **94**, 586
- Oshagh M., Santos N. C., Ehrenreich D., Haghighipour N., Figueira P., Santerne A., Montalto M., 2014, *A&A*, **568**, A99
- Parviainen H., Pallé E., Nortmann L., Nowak G., Iro N., Murgas F., Aigrain S., 2016, *A&A*, **585**, A114
- Pearson K. A., Griffith C. A., Zellem R. T., Koskinen T. T., Roudier G. M., 2019, *AJ*, **157**, 21
- Pinhas A., Madhusudhan N., 2017, *MNRAS*, **471**, 4355
- Pinhas A., Madhusudhan N., Gandhi S., MacDonald R., 2019, *MNRAS*, **482**, 1485
- Pont F., Sing D. K., Gibson N. P., Aigrain S., Henry G., Husnoo N., 2013, *MNRAS*, **432**, 2917
- Rackham B. V., Apai D., Giampapa M. S., 2018, *ApJ*, **853**, 122

- Rackham B. V., Apai D., Giampapa M. S., 2019, *AJ*, **157**, 96
- Rasmussen C. E., Williams C. K. I., 2006, *Gaussian Processes for Machine Learning*
- Rosich A., Herrero E., Mallonn M., Ribas I., Morales J. C., Perger M., Anglada-Escudé G., Granzer T., 2020, *A&A*, **641**, A82
- Schlaflly E. F., Finkbeiner D. P., 2011, *ApJ*, **737**, 103
- Schwarz G., 1978, *Ann. Statist.*, **6**, 461
- Seager S., Mallén-Ornelas G., 2003, *ApJ*, **585**, 1038
- Seager S., Sasselov D. D., 2000, *ApJ*, **537**, 916
- Sedaghati E., et al., 2017, *Nature*, **549**, 238
- Sing D. K., et al., 2011, *MNRAS*, **416**, 1443
- Sing D. K., et al., 2013, *MNRAS*, **436**, 2956
- Sing D. K., et al., 2016, *Nature*, **529**, 59
- Smith A. M. S., et al., 2014, *A&A*, **570**, A64
- Sousa S. G., et al., 2018, *A&A*, **620**, A58
- Southworth J., 2011, *MNRAS*, **417**, 2166
- Stevenson K. B., 2016, *ApJ*, **817**, L16
- Tody D., 1993, in Hanisch R. J., Brissenden R. J. V., Barnes J., eds, *Astronomical Society of the Pacific Conference Series Vol. 52, Astronomical Data Analysis Software and Systems II*. p. 173
- Tsiaras A., et al., 2018, *AJ*, **155**, 156
- Wakeford H. R., Sing D. K., 2015, *A&A*, **573**, A122
- Wakeford H. R., et al., 2017a, *Science*, **356**, 628
- Wakeford H. R., Visscher C., Lewis N. K., Kataria T., Marley M. S., Fortney J. J., Mandell A. M., 2017b, *MNRAS*, **464**, 4247
- Weaver I. C., et al., 2020, *AJ*, **159**, 13
- Welbanks L., Madhusudhan N., Allard N. F., Hubeny I., Spiegelman F., Leininger T., 2019, *ApJ*, **887**, L20
- Woitke P., Helling C., Hunter G. H., Millard J. D., Turner G. E., Worters M., Blecic J., Stock J. W., 2018, *A&A*, **614**, A1
- Wong I., et al., 2020, *AJ*, **159**, 234
- Zacharias N., et al., 2015, *AJ*, **150**, 101
- Zahnle K., Marley M. S., Freedman R. S., Lodders K., Fortney J. J., 2009, *ApJ*, **701**, L20
- Zhang X., 2020, *Research in Astronomy and Astrophysics*, **20**, 099
- Zhang M., Chachan Y., Kempton E. M. R., Knutson H. A., 2019, *PASP*, **131**, 034501
- Zhang M., Chachan Y., Kempton E. M. R., Knutson H. A., Chang W. H., 2020, *ApJ*, **899**, 27

AFFILIATIONS

- ¹Key Laboratory of Planetary Sciences, Purple Mountain Observatory, Chinese Academy of Sciences, Nanjing 210023, PR China
- ²Instituto de Astrofísica de Canarias, Vía Láctea s/n, E-38205 La Laguna, Tenerife, Spain
- ³Departamento de Astrofísica, Universidad de La Laguna, Spain
- ⁴Key Laboratory of Radio Astronomy, Purple Mountain Observatory, Chinese Academy of Sciences, Nanjing 210023, PR China
- ⁵Max-Planck-Institut für Astronomie, Königstuhl 17, 69117 Heidelberg, Germany
- ⁶Institut für Astrophysik, Georg-August-Universität, Friedrich-Hund-Platz 1, D-37077 Göttingen, Germany
- ⁷Science Support Office, Directorate of Science, European Space Research and Technology Centre (ESA/ESTEC), Keplerlaan 1, 2201 AZ Noordwijk, The Netherlands
- ⁸Department of Earth and Planetary Science, Graduate School of Science, The University of Tokyo, Japan
- ⁹MTA-ELTE Exoplanet Research Group, 9700 Szombathely,

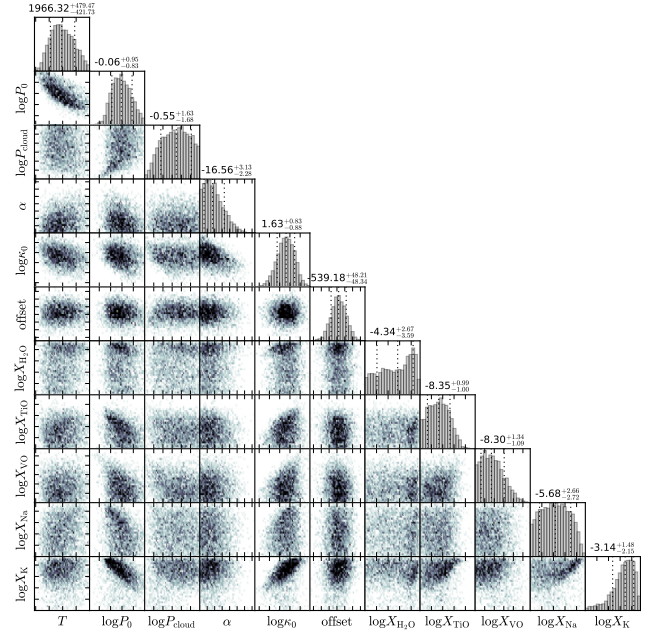


Figure A1. Corner plot for the spectral retrieval analysis performed with *petitRADTRANS*, where no spot contamination is considered.

Szent Imre h. u. 112, Hungary

¹⁰*ELTE Gothard Astrophysical Observatory, 9700 Szombathely, Szent Imre h. u. 112, Hungary*

¹¹*Astronomical Institute, Slovak Academy of Sciences, 05960 Tatranská Lomnica, Slovakia*

¹²*Institute of Planetary Research, German Aerospace Center, Rutherfordstrasse 2, 12489 Berlin, Germany*

¹³*Astrobiology Center of NINS, 2-21-1, Osawa, Mitaka, Tokyo 181-8588, Japan*

¹⁴*National Astronomical Observatory of Japan, 2-21-1 Osawa, Mitaka, Tokyo 181-8588, Japan*

¹⁵*Department of Astronomy, The University of Tokyo, 7-3-1 Hongo, Bunkyo-ku, Tokyo 113-0033, Japan*

¹⁶*Komaba Institute for Science, The University of Tokyo, 3-8-1 Komaba, Meguro, Tokyo 153-8902, Japan*

¹⁷*Japan Science and Technology Agency, PRESTO, 3-8-1 Komaba, Meguro, Tokyo 153-8902, Japan*

¹⁸*Department of Astronomical Science, The Graduated University for Advanced Studies, SOKENDAI, 2-21-1, Osawa, Mitaka, Tokyo, 181-8588 Japan*

¹⁹*Institute of Astronomy and Astrophysics, Academia Sinica, P.O. Box 23-141, Taipei 10617, Taiwan, R.O.C.*

²⁰*Department of Astrophysics, National Taiwan University, Taipei 10617, Taiwan, R.O.C.*

APPENDIX A: ADDITIONAL TABLES AND FIGURES

This paper has been typeset from a \LaTeX file prepared by the author.

Table A1. Mid-transit times of WASP-104b.

Epoch	Mid-transit time (BJD _{TDB} - 2450000)	Residuals (sec)	Instrument
-885	6381.536026 ± 0.000406	-19.0	TRAPPIST
-881	6388.558002 ± 0.000786	11.5	TRAPPIST
-877	6395.578120 ± 0.000751	-118.5	TRAPPIST
-873	6402.601347 ± 0.000192	20.1	Euler
-869	6409.622108 ± 0.000457	-54.3	Euler
-848	6446.485884 ± 0.000328	-32.1	TRAPPIST
-494	7067.899763 ± 0.000149	-7.3	DBSP
-16	7906.983803 ± 0.000069	5.6	K2
-15	7908.739168 ± 0.000069	2.1	K2
-14	7910.494656 ± 0.000058	9.2	K2
-13	7912.250033 ± 0.000058	6.7	K2
-12	7914.005334 ± 0.000056	-2.3	K2
-11	7915.760811 ± 0.000061	3.9	K2
-10	7917.516096 ± 0.000063	-6.6	K2
-9	7919.271501 ± 0.000058	-6.6	K2
-8	7921.026996 ± 0.000063	1.1	K2
-7	7922.782210 ± 0.000070	-15.4	K2
-6	7924.537710 ± 0.000115	-7.3	K2
-5	7926.293033 ± 0.000072	-14.4	K2
-4	7928.048514 ± 0.000063	-8.0	K2
-3	7929.803990 ± 0.000060	-1.8	K2
-2	7931.559450 ± 0.000074	2.8	K2
-1	7933.314857 ± 0.000064	3.0	K2
0	7935.070336 ± 0.000100	9.3	K2
1	7936.825603 ± 0.000057	-2.7	K2
2	7938.580941 ± 0.000087	-8.5	K2
3	7940.336465 ± 0.000073	1.7	K2
4	7942.091794 ± 0.000062	-4.9	K2
5	7943.847253 ± 0.000081	-0.3	K2
6	7945.602633 ± 0.000057	-2.5	K2
7	7947.358142 ± 0.000072	6.4	K2
8	7949.113446 ± 0.000072	-2.4	K2
9	7950.868920 ± 0.000057	3.6	K2
10	7952.624273 ± 0.000065	-1.0	K2
11	7954.379661 ± 0.000057	-2.5	K2
12	7956.135168 ± 0.000060	6.2	K2
13	7957.890516 ± 0.000060	1.2	K2
14	7959.645980 ± 0.000070	6.4	K2
15	7961.401285 ± 0.000082	-2.4	K2
16	7963.156847 ± 0.000060	11.1	K2
17	7964.912183 ± 0.000071	5.1	K2
18	7966.667603 ± 0.000071	6.3	K2
19	7968.422901 ± 0.000070	-3.0	K2
20	7970.178242 ± 0.000071	-8.5	K2
21	7971.933684 ± 0.000084	-5.4	K2
22	7973.689231 ± 0.000071	6.8	K2
23	7975.444730 ± 0.000065	14.9	K2
24	7977.199945 ± 0.000090	-1.5	K2
25	7978.955214 ± 0.000080	-13.4	K2
26	7980.710816 ± 0.000081	3.5	K2
27	7982.466215 ± 0.000063	3.0	K2
28	7984.221461 ± 0.000062	-10.8	K2
112	8131.675595 ± 0.000131	-5.5	MuSCAT2
120	8145.719154 ± 0.000151	21.6	MuSCAT2
162	8219.445487 ± 0.000537	-39.2	MuSCAT2
166	8226.467854 ± 0.000120	25.2	MuSCAT2
296	8454.669836 ± 0.000204	-39.6	MuSCAT2
300	8461.691865 ± 0.000191	-4.5	MuSCAT2
304	8468.713529 ± 0.000114	-0.9	MuSCAT2
308	8475.735175 ± 0.000115	1.1	MuSCAT2
329	8512.598795 ± 0.000118	10.0	MuSCAT2
391	8621.433868 ± 0.000225	3.4	MuSCAT2
546	8893.521531 ± 0.001371	-14.7	MuSCAT2
558	8914.586463 ± 0.000148	-9.2	MuSCAT2
562	8921.608071 ± 0.000147	-10.4	MuSCAT2
567	8930.384955 ± 0.000211	-22.9	MuSCAT2

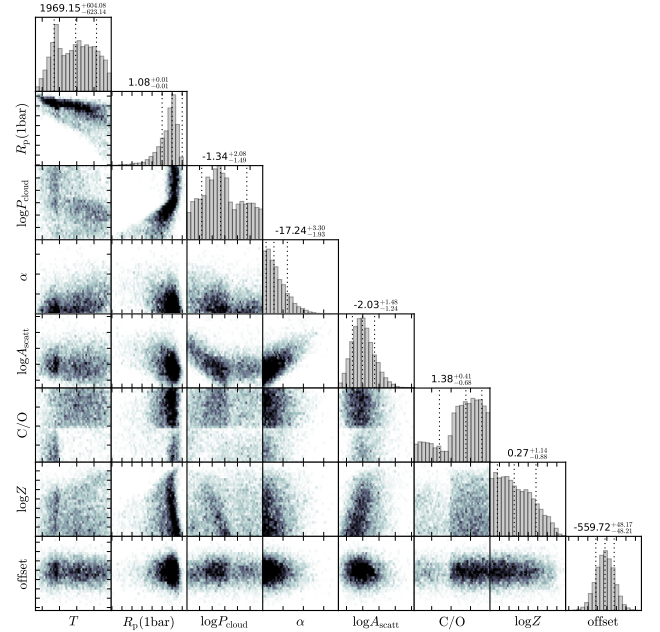


Figure A2. Corner plot for the spectral retrieval analysis performed with PLATON, where no spot contamination is considered.

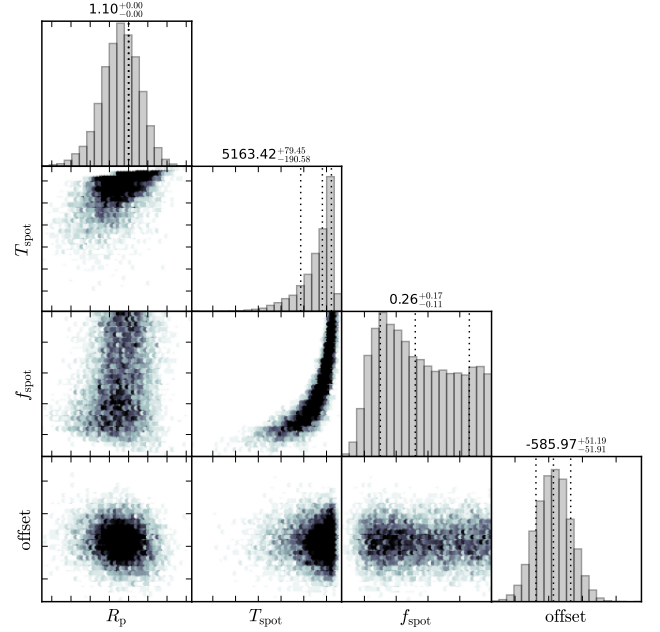


Figure A3. Corner plot for the spectral retrieval analysis performed with PLATON, where spot contamination is the only slope origin.